



Effect of carbon addition on the microstructure and corrosion resistance of the CoCrFeNi high-entropy alloy

Xueming Wei^a, Lijun Zhang^{a,*}, Fengyi Zhang^a, Chunzhi Zhang^a, Qixiang Jia^{b,*}, Kai Sun^{c,*}, Dongtao Duan^c, Hui Jiang^d, Gong Li^e

^a School of Materials Science and Engineering, Shandong University of Science and Technology, Qingdao, Shandong 266590, PR China

^b College of Intelligent Equipment, Shandong University of Science and Technology, Taian, Shandong 271001, PR China

^c Jining Luoling new mineral products Co., LTD, Jining, Shandong 273516, PR China

^d College of Mechanical and Electronic Engineering, Shandong University of Science and Technology, Qingdao, Shandong 266590, PR China

^e State Key Laboratory of Metastable Materials Science and Technology, Yanshan University, Qinhuangdao, Hebei 066004, PR China

ARTICLE INFO

Keywords:

High-entropy alloy
Carbon atom
Microstructure
Passive film

ABSTRACT

Interstitial atom doping can enhance mechanical properties and phase structure, but its impact on corrosion resistance is not well-researched. This study investigated the influence of carbon-doping on the microstructure and corrosion resistance of CoCrFeNi high-entropy alloys. The results show that alloy doped with a moderate carbon content (C0.3 alloy) have the best corrosion resistance in 3.5 wt% NaCl solution, while alloys with carbides (M_7C_3) show poor corrosion resistance. The stability, semiconductive property, and composition of the passivation films were characterized to reveal the corrosion mechanisms. These findings provide a theoretical basis for the development and application of carbon-doped high-entropy alloys.

1. Introduction

Traditional alloy design usually selects one or two elements as the main grouping and then adds small amounts of other elements to improve the alloy properties, such as aluminium alloys, titanium alloys, magnesium alloys, nickel-based high temperature alloys and stainless steel. However, traditional alloy design is limited to the understanding of the information at the apex and edges of the phase diagram, while the alloys at the centre of the phase diagram are less understood. Moreover, one or two elements as the dominant element limits the degree of freedom in alloy composition, thus restricting the further development of special alloy microstructures, properties and applications. It's urgent to need new type of alloys to meet the growing industrial demand. In 2004, Taiwanese scholars [1] proposed a new alloy preparation concept. These new multi-principal elements alloys were named as 'high-entropy alloys (HEAs)' because of their significantly higher mixing entropies than conventional alloys. HEAs have four major effects compared to conventional alloys including high-entropy effect [2], hysteresis diffusion effect [3,4], lattice distortion effect [5,6] and cocktail effect. The four major effects regarding HEAs are described in detail by Zhang et al. [7]. Higher mixed entropy values can reduce or inhibit the emergence of

intermetallic compounds and the second phases according to the Gibbs free energy formula [8], making it easier for atoms in HEAs to form stable solid solutions [9]. The coupling of multiple mechanisms attributed to the unique compositional and structural features of HEAs [7,9, 10] make these alloys having superior strength [11], excellent toughness [12], better wear [13] and corrosion resistance [14], and better application prospect in naval equipment [15], aerospace [16] and other aspects [17].

Corrosion has also been an important issue limiting the application of metallic materials [18]. How to obtain materials with excellent mechanical properties and corrosion resistance has attracted the attention of many researchers. Elemental alloying has proved to be an effective way to improve the properties of HEAs. Two broad classes of atoms are added to improve the corrosion resistance of HEAs. One group consists of large-sized atoms that are present in the alloy as replacement atoms or forming a second phase, such as Al [19], Nb [20], Cu [21], Zr [22], Mo [23], Ti [24] etc. Shi et al. [25] studied the corrosion performance of the $Al_xCoCrFeNi$ ($x = 0.3, 0.5, 0.7$) HEAs, and their results showed that the high Al content could increase the volume fraction of the BCC phase rich in (Al, Ni) and depleted in Cr, making the alloys susceptible to Cl⁻ erosion and reducing their resistance to local corrosion. Zhao et al. [26]

* Corresponding authors.

E-mail addresses: zhanglijun077@163.com (L. Zhang), Qixiangjia992@163.com (Q. Jia), 13675370099@139.com (K. Sun).

found that the increase of Al content in the $\text{Al}_x\text{CrFeNi}_{3-x}$ alloy led to the content of Cr_2O_3 as the main contributor to corrosion resistance in the passivation film decrease, and the content of loose and porous Al_2O_3 increase. Wang et al. [27] found that the corrosion resistance of the $\text{AlCrFeNi}_3\text{Cu}_x$ HEAs presents a trend of increasing and then decreasing with increasing the Cu content. The best corrosion resistance of the $\text{AlCrFeNi}_3\text{Cu}_{0.4}$ alloy is due to the formation of the Cr-rich BCC precipitates in the B_2 matrix leading to generate a dense Cr_2O_3 passivation film. Liu et al. [28] prepared the FeCoCrNiNb_x HEAs, and the corrosion tests results showed that these Nb-added alloys had wider passivation intervals and lower corrosion current densities than 316 L stainless steels. The alloying of large-sized atoms has been studied extensively and the research has become more mature.

Another group of small-sized atoms, such as C [29,30], B [31], N [32], O [33], etc., are often doped in the HEAs as interstitial atoms or forming a second phase. Current researches mostly focused on the influence of the small-sized atoms addition on mechanical properties. For instance, Lei et al. [34] prepared the optimal oxygen-doped variant $(\text{TiZrHfNb})_{98}\text{O}_2$ alloy, and they found that the addition of 2.0 at% oxygen improved both the strength and plasticity, which was mainly attributed to the fact that the oxygen occupies the interstitial sites in the Zr and/or Ti-rich group clusters in an ordered manner. Xie et al. [35] prepared the CoCrFeNiMn HEA with the addition of 0.1 at% N and observed an increase in both the strength and ultimate compressive strength compared to the CoCrFeNiMn HEA produced by the same method. This shows that adding N element is a feasible method for enhancing the properties of HEAs. Doping interstitial atoms as a means of alloying can effectively regulate the phase structure of high-entropy alloys and improve their mechanical properties. However, there is a lack of in-depth research on the effect of interstitial atoms on the corrosion resistance and corrosion mechanism of high-entropy alloys. It is necessary to explore the effect of interstitial atoms on the corrosion resistance of the HEAs.

In our previous work [36], we explored the effect of carbon content on the mechanical properties of the CoCrFeNi HEA and found that the addition of carbon atoms could effectively improve the mechanical properties of the alloys. In this paper, a series of CoCrFeNiC_x ($x = 0.1, 0.2, 0.3, 0.5$, and 0.9 , wt%) HEAs were synthesized to investigate carbon alloying effects on the microstructure and corrosion performance. The micro-morphological evolution and phase composition of the HEAs were explored by thermodynamic parameters, scanning electron microscopy (SEM), X-ray diffraction (XRD), and transmission electron microscopy (TEM) techniques. The effect of carbon content on the corrosion resistance and electronic properties (carrier density and diffusion coefficient) of the passivation film was also investigated by electrochemical tests such as Impedance Spectroscopy (EIS), Potentiodynamic Polarization (TAFEL) curves, Constant Potential Polarization (CPP) curves and Mott-Schottky (M-S) curves. The effect of carbon content on the composition of the passivation films was further investigated by X-ray photoelectron spectroscopy (XPS) technique. The surface morphology and different phase potential distributions were obtained by scanning Kelvin probe microscopy (SKPFM). Our results can provide a good reference for the development of new corrosion-resistant HEAs.

2. Experiment procedures

2.1. Alloy preparation

A series of CoCrFeNiC_x ($x = 0.1, 0.2, 0.3, 0.5$, and 0.9 , wt%) HEAs were prepared by arc melting method in a vacuum arc melting furnace, after which the well-mixed liquid metal was drawn into a water-cooled copper mold to obtain ingots. The HEAs prepared using $0.1, 0.2, 0.3, 0.5$, and 0.9 wt% carbon, which were labeled as C0.1, C0.2, C0.3, C0.5, and C0.9 alloys, respectively. In order to ensure the homogeneity of the components and chemical composition, these alloy ingots were remelted not less than five times.

The ingots were cut into $10 \times 10 \times 3$ mm³ metal blocks by wire electrode discharge machining. The surfaces of these samples were ground using 3000 grit sandpaper, which was followed by polishing using a $1.0 \mu\text{m}$ diamond paste. The polished samples were etched using an aqua-regia solution for microstructural characterization afterwards.

2.2. Microstructure characterization

The phase structure of the CoCrFeNiC_x ($x = 0.1, 0.2, 0.3, 0.5$, and 0.9 , wt%) HEAs was analyzed using an X-ray diffractometer (XRD, Rigaku D/MAX2500PC) with the Cu K α radiation ($\lambda = 1.54 \text{ \AA}$) at 40 kV, a current of 40 mA, diffraction range of $20\text{--}100^\circ$, and diffraction rate of $5^\circ/\text{min}$. The microstructure and elemental distribution of these alloys were employed on a field emission scanning electron microscope (SEM, Nova Nono SEM 450) with Energy Disperse Spectroscopy (EDS) and transmission electron microscopy (TEM, FEI Talos F200X).

2.3. Electrochemical measurements

The electrochemical measurements were carried out on an electrochemical workstation (CHI 760e) with a typical three-electrode system in 3.5 wt% NaCl solution. A standard three-electrode system consists of platinum sheet as the counter electrode, a saturated calomel electrode (SCE) as the reference electrode, and the test sample as the working electrode. Before the tests, open circuit potential (OCP) was monitored for 3600 s to reach a steady state. Immediately, the EIS measurements were conducted under OCP condition, where the frequency ranged from 10^5 Hz to 10^{-2} Hz with an amplitude of 10 mV. The ZsimpWin software was adopted to obtain the equivalent circuit and fit the EIS data. Next, the potentiodynamic polarization tests were performed from -1 V to 2.0 V (vs. SCE). The scanning rate was set to 5 mV/s, and the corrosion parameters such as corrosion potential (E_{corr}), corrosion current density (I_{corr}), passivation current density (I_{pass}) and pitting potential (E_{pit}) were obtained via fitting the polarization curves. The micro-morphology of the samples after the potentiodynamic polarization tests was characterized by the Nova Nono SEM 450 microscope.

In order to further obtain the effect of carbon content on the corrosion resistance of the alloys, we selected C0.1, C0.3, and C0.9 HEAs with different carbon contents as the objects of the next study according to their microscopic morphology and corrosion resistance. Potentio-static passivation experiments were performed to obtain the steady-state current density (I_{ss}) and to clarify the kinetic processes of film growth and dissolution. The imposed potentials of -0.3 V, -0.2 V, -0.1 V, and 0 V (vs. SCE) were selected according to the potentiodynamic curves and applied for 3600 s. The I_{ss} was obtained from the average value at the end of each current-time transient curve. After the samples initially polarized at a specific anodic potential for 1 hour, EIS measurements were carried out in the frequency range from 10^5 Hz to 10^{-2} Hz with an amplitude of 10 mV. The ZsimpWin software was adopted to fit the EIS data. The Mott-Schottky (M-S) measurements were conducted to explore the semiconductor characteristics of the passive films at a fixed frequency of 1000 Hz with a potential scanning rate of 50 mV/step from -1 V to 1 V (vs. SCE). The sweeping rate employed here was sufficiently fast to satisfy the assumption of “frozen-in defect structure” for the Mott-Schottky theory. All the electrochemical measurements were carried out at room temperature, and repeated at least three times to maintain the reproducibility.

2.4. Passive films analysis

The composition of the alloy passivation film was analyzed using an X-ray photoelectron spectrometer (XPS) (Thermo SCIENTIFIC ESCALAB Xi⁺, Al K α x-ray source, $h\nu = 1486.68$ eV). Before the measurements, the potentio-static tests were firstly conducted at -1.0 V (vs. SCE) for 300 s to remove the surface oxide films formed in the air and then conducted at 0 V (vs. SCE) for 3600 s to obtain stable films in the 3.5 wt% NaCl

solution. All the peaks were calibrated with a standard C1s peak at 284.8 eV. Avantage software was used for data processing and peak fitting of the experimental results.

2.5. SKPFM measurement

To obtain the surface potential distribution of the carbide-containing HEAs, Scanning Kelvin probe force microscopy (SKPFM) (Bruker Dimension Icon AFM) was used to scan the sample surface and measure the local contact potential difference (V_{CPD}) with a Pt/Ir coated probe.

3. Results

3.1. Phase identification and microstructural evolution

In the interest of predicting the effect of carbon content on the microscopic morphology and phase composition of CoCrFeNi HEA, the enthalpy of mixing of the constituent elements of the alloy is presented in Fig. 1. The figure shows that the mixing enthalpy between metal atoms and carbon atoms is more negative than that between metal atoms. This indicates that the metal atoms are more likely to produce new carbide phases that are different from the matrix phase, which signifies that the CoCrFeNi_x ($x = 0.1, 0.2, 0.3, 0.5$, and 0.9 , wt%) HEAs may evolve from single-phase to multi-phase with the increase of the carbon content. As the mixing enthalpy of Cr and C atoms in a metal atom is the most negative, the second phase is most likely to be a carbide containing the high Cr content.

The XRD patterns of the CoCrFeNi_x ($x = 0.1, 0.2, 0.3, 0.5$, and 0.9 , wt%) HEAs are shown in Fig. 2(a). The results indicate that the FCC phase is the primary phase in these HEAs. An increase in carbon content led to the emergence of a minor reflection peak, indicating the formation of M₇C₃-type carbides. This indicates that the increase in carbon content leads to an evolution of the phase composition of the present HEAs from FCC to FCC+M₇C₃, which is consistent with the predicted results of thermodynamic parameters. The enlarged image of (111) crystal surface of the FCC phase is shown on the right side of Fig. 2(a), from which it can be seen that the (111) peak moves to the left side as the carbon content increasing from 0.1 wt% to 0.3 wt%. A further increase in the carbon content caused the (111) peak to shift to the right side. The lattice constants of the FCC phase in the current HEAs are determined from their (111) peaks, as depicted in Fig. 2(b). The lattice constants increase

with a rise in the carbon content up to 0.3 wt%, suggesting that the carbon atoms dissolved in the interstitial sites of the FCC phase. However, the lattice constant of the FCC phase decrease as the carbon content increase to 0.5 wt% or 0.9 wt%, indicating that the formation of the carbides reduced the solid-solution limit of the carbon content in the FCC phase.

Fig. 3(a)-(f) show the high magnification SEM images of the CoCrFeNi_x ($x = 0.1, 0.2, 0.3, 0.5$, and 0.9 , wt%) HEAs, respectively. The C0.1, and C0.2 HEAs are single FCC phase alloys with large grain sizes, as shown in Fig. 3(a)-(b). As can be observed from Fig. 3(c), the C0.3 HEA shows the appearance of island-like carbide precipitates on the grain boundaries. Fig. 3(d)-(e) show that a further increase of the carbon content leads to the precipitation of a bright white eutectic-like second phase at the grain boundaries of C0.5 and C0.9 alloys. Combined with the XRD results, the bright white slaty phase is the M₇C₃ phase and the metallic matrix is the FCC phase. In order to further obtain the distribution of the elements in the alloy, we have also characterized the distribution condition of the constituent elements by using the EDS attached to the SEM microscope. The distribution of the constituent elements of C0.9 HEA is shown in Fig. 4. The gray-black matrix of the alloy is a Co-, Fe- and Ni-rich FCC phase, and the bright white M₇C₃ is a Cr- and C-rich phase. The energy spectrum analysis results agree with the thermodynamic phase composition prediction.

In order to further investigate the crystal structure of HEA phase composition, the TEM images of C0.9 HEA were obtained. Fig. 5 shows the bright field image of the C0.9 HEA as well as the selected area electron diffraction (SAED) maps of the FCC phase and M₇C₃ phase. The bright field image of the C0.9 alloy [see Fig. 5(a)] presents that the eutectic-like region consists of the lath-like M₇C₃ phase and the inter-lath FCC phase. In order to determine the composition of M₇C₃, we obtained the energy spectrum results from TEM. The elemental composition results show that the M₇C₃ phase contain 26.98 % C, 3.20 % Co, 62.59 % Cr, 6.00 % Fe and 1.23 % Ni, which is consistent with the atomic ratio of M₇C₃ phase (M represents Cr, Fe, Co, Ni elements). Fig. 5 (b) shows the high-resolution TEM image of the FCC phase and M₇C₃ phase, and Fig. 5(1–3) show the selected area electron diffraction (SAED) images of the FCC phase and the M₇C₃ carbide in different regions of Fig. 5(b). Fig. 5(1) shows the Fourier diffraction pattern at the two-phase phase boundary, which indicates that the orientation relationship between the M₇C₃ precipitate and FCC matrix are (020)_{FCC}// (011-0)_{M7C3} and [001]_{FCC}//[21-1-0]_{M7C3}. The SAED pattern along the [001] zone axis indicated that the alloy matrix showed an FCC crystal structure in Fig. 5(2). The SAED pattern along the [2110] zone axis indicated that the M₇C₃ carbides had a hexagonal structure with the P31c space group [37,38]. The lattice parameters a and c are about 1.3992 and 0.4533 nm, respectively.

3.2. Electrochemical corrosion behavior

The kinetic potential polarization technique is an important technique for corrosion resistance evaluation of alloys. The corrosion parameters analyzed from the kinetic potential polarization curves can help us understand the nodes and processes of corrosion [39,40]. Fig. 6 shows the results of kinetic potential polarization curves of the CoCrFeNi_x ($x = 0.1, 0.2, 0.3, 0.5$, and 0.9 , wt%) HEAs in 3.5 wt% NaCl solution. The images show that these alloys exhibit passivation behavior indicating the good passivation properties of the present HEAs in 3.5 wt % NaCl solution.

It is obvious that the cathode region of the polarization curves almost overlaps together, revealing that the change of compositions for the current HEAs have no significant impact on the cathodic process. Typical passive regions with no activation-passive transition regions are found in the anodic region, indicating that the HEAs could spontaneously passivate in the electrolyte solution. In the anodic polarization process, the HEAs with different carbon content show the same passivation interval and the corrosion current density of the alloys basically

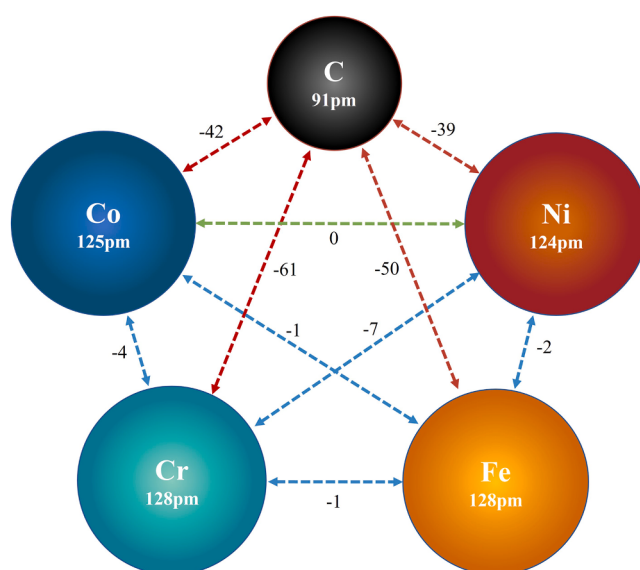


Fig. 1. The mixing enthalpy of different atom pairs in the present alloys (kJ/mol).

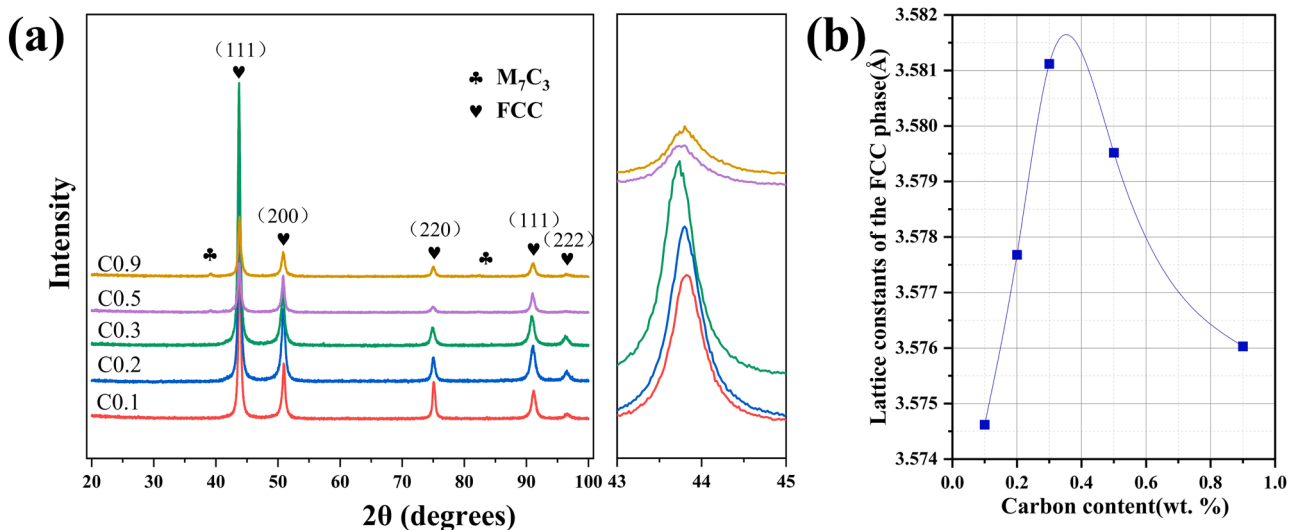


Fig. 2. (a) XRD patterns of the CoCrFeNiC_x HEAs with different carbon content. The insert shows the high magnification images of the (111) peak of the FCC phase. (b) The lattice constants of the FCC phase versus carbon content of the present HEAs.

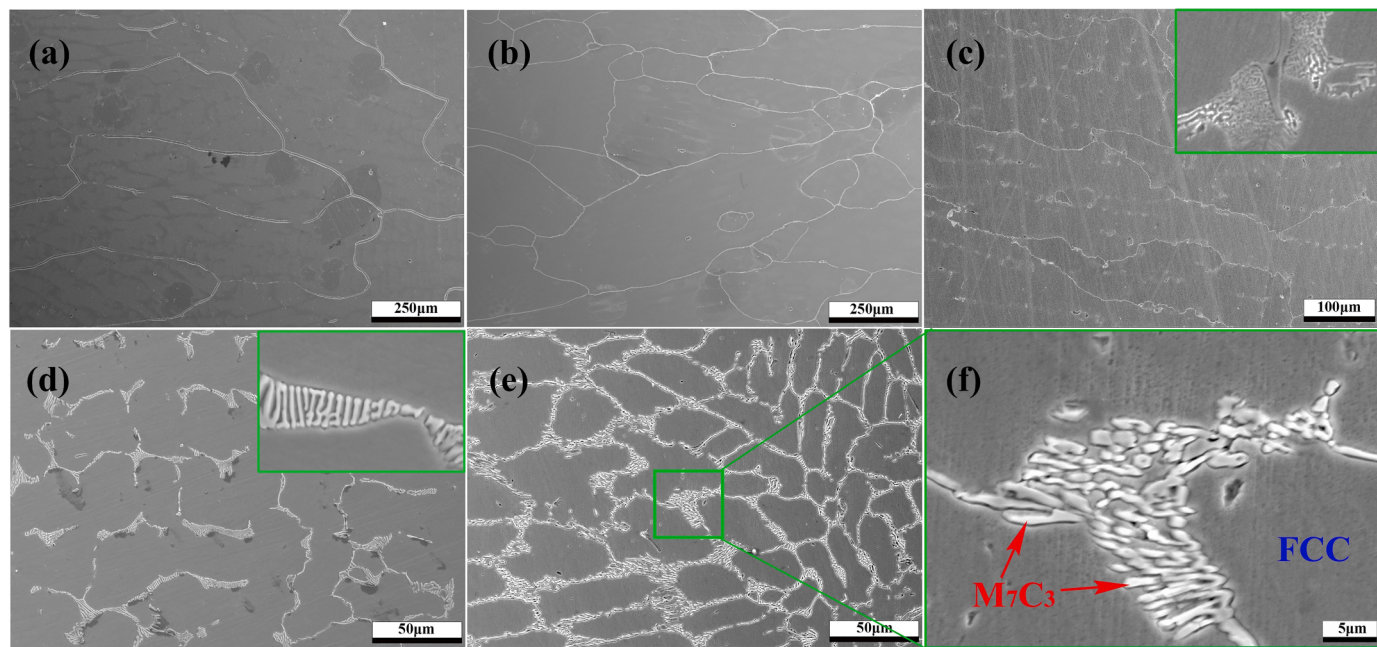


Fig. 3. SEM images of the C0.1 (a), C0.2 (b), C0.3 (c), C0.5 (d), and C0.9 (e) HEAs. (f) is local magnified of (e).

remains unchanged with in the passivation interval indicating that the HEAs are able to form stable passivation films in the 3.5% NaCl solution. Compared to C0.1, C0.2, and C0.3 HEAs, C0.5 and C0.9 HEAs exhibit higher critical pitting potential. The addition of carbon reduces the local corrosion resistance of the HEAs. The passivation films of C0.5 and C0.9 HEAs experience sub-steady-state pitting on their surface, which transitions into steady-state pitting, ultimately leading to the breakdown of the passivation film and a rapid increase in current. The self-corrosion potential (E_{corr}), corrosion current density (i_{corr}), passivation current density (i_{pass}), critical pitting potential (E_{pit}) and passivation potential ($\Delta E = E_{pit} - E_{corr}$) are obtained by analyzing the potential polarization curves, as summarized in Table 1.

Table 1 shows that the values of E_{corr} present an increasing and then decreasing trend with increasing the carbon content. Among them, C0.3 alloy has the largest E_{corr} value of -0.460 V (vs SCE). The addition of appropriate amount of carbon is beneficial to optimize the corrosion

resistance of the metal as observed in the thermodynamic perspective of corrosion occurrence. In the evaluation of corrosion resistance of non-passivated alloys, the dimensional passivation current density is an important corrosion parameter [41]. The i_{pass} values reflected the diffusion rates of the ions through the passive films, i.e., the dissolution rate of the passive films. The i_{pass} value decreases and then increases with the increase of carbon content, as shown in Table 1. The C0.3 alloy has the smallest i_{pass} value of $5.774 \mu\text{A cm}^{-2}$, indicating that this alloy has the lowest dissolution rate of passivation film and the best corrosion resistance in 3.5% NaCl solution.

The E_{pit} value of C0.5 alloy is less than that of C0.9 alloy which means that the localized corrosion resistance of C0.9 alloy is worse as compared to C0.5 alloy. The difference between the pitting potential and the self-corrosion potential (ΔE) is used to characterize the resistance to pitting nucleation in assessing the corrosion resistance of the alloy. C0.2 HEA exhibits superior pitting resistance than C0.3 HEA. The decrease in

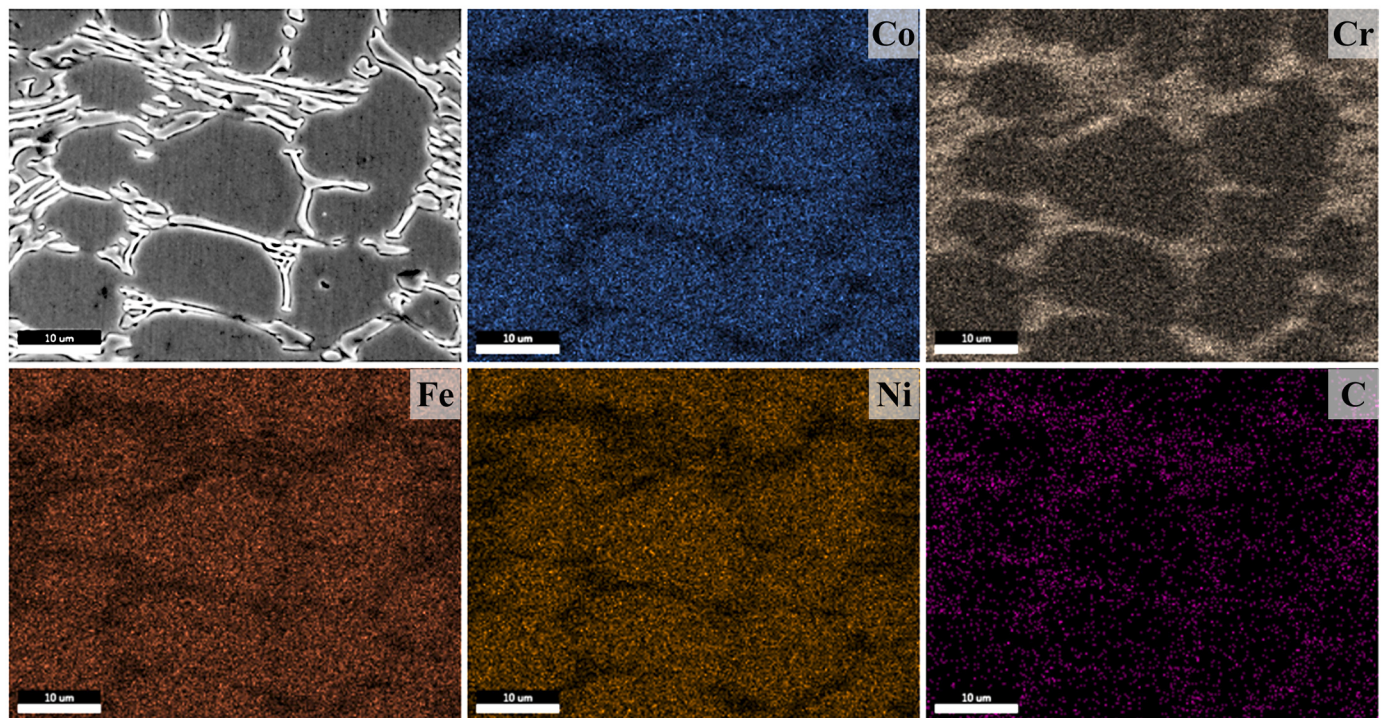


Fig. 4. Element distribution mapping of the C0.9 HEA.

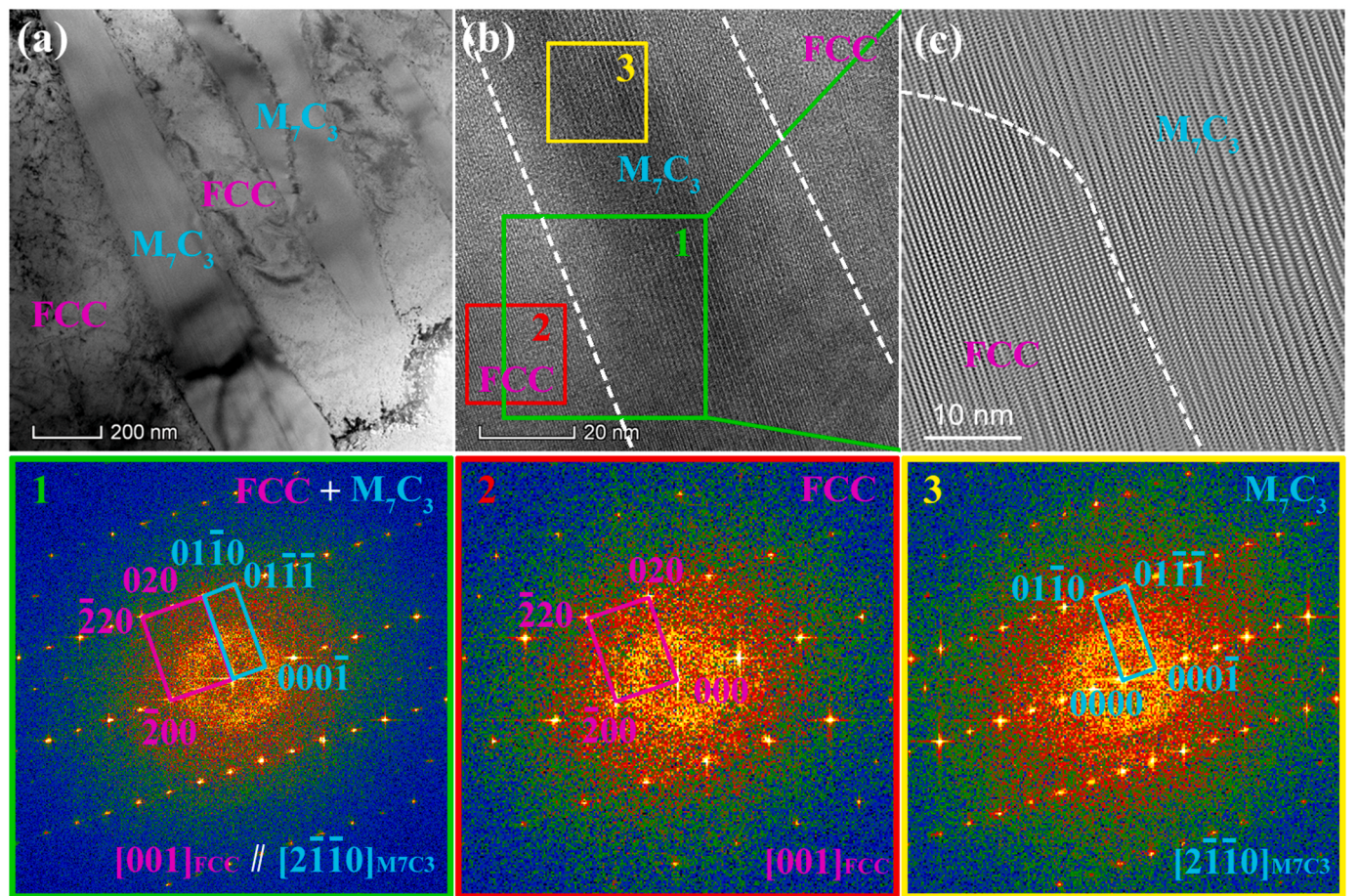


Fig. 5. (a) The bright-field TEM image of the C0.9 HEA, (b) The HRTEM image in the interface region between the FCC matrix and M_7C_3 phase, and the corresponding FFT patterns at different zone are also presented. (c) Inverse FFT image of partial enlarged view in (b).

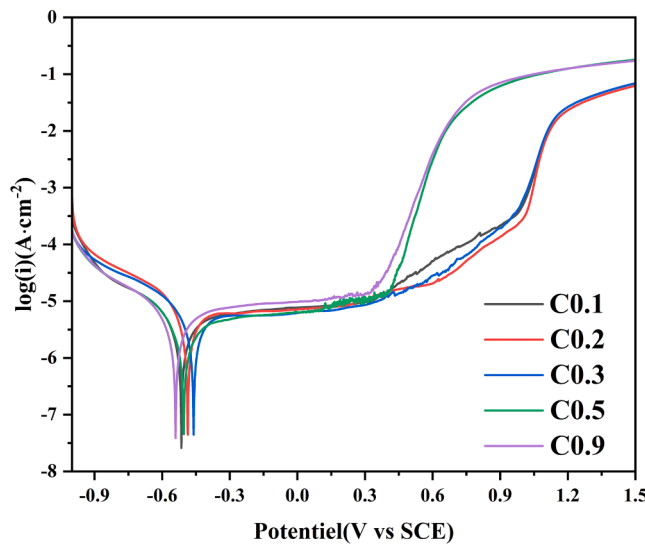


Fig. 6. The potentiodynamic polarization curves of the CoCrFeNiC_x HEAs with different carbon content in 3.5 wt% NaCl solution at room temperature.

Table 1
Electrochemical parameters in 3.5 wt% NaCl solution from potential polarization curves.

Alloys	E_{corr} (V/SCE)	I_{corr} ($\mu A/cm^2$)	i_{pass} ($\mu A/cm^2$)	E_{pit} (V/SCE)	ΔE (V)
C0.1	-0.515	2.168	7.248	0.848	1.363
C0.2	-0.486	3.258	6.645	1.016	1.502
C0.3	-0.460	2.754	5.774	1.002	1.462
C0.5	-0.504	1.683	5.806	0.413	0.917
C0.9	-0.540	2.432	9.214	0.368	0.908

pitting resistance of the C0.9 alloy compared to C0.5 is strongly related to the increase in the volume fraction of the second carbide phase and the decrease in the chromium content of the FCC matrix. It is also demonstrated that the addition of excess carbon leads to a decrease in the localized corrosion resistance of the alloy.

3.3. Impedance spectrum analysis

EIS, a valuable tool for studying corrosion properties, was utilized to characterize the electrochemical corrosion processes of the alloy surface

[42,43].

Fig. 7 shows the Nyquist and Bode plots of the present HEAs under the OCP conditions in 3.5 wt% NaCl solution. In Fig. 7(a), all of the alloys present the same half-arcs, indicating that the increase of the carbon content does not result in a change in the passivation mechanism of these alloys [44]. The radius of the half arc in the Nyquist diagram directly reflects the corrosion resistance of the material [45,46], and the larger the diameter of the half arc also indicates that the corrosion resistance of the material is better. Obviously, the maximum semi-circular diameter of the C0.3 alloy confirms that the corrosion resistance of C0.3 in 3.5% NaCl solution is the best. The impedance semi-circular arc diameters of C0.5 and C0.9 alloys show a significant decrease, which indicates that the addition of high carbon content is detrimental to the improvement of the corrosion resistance of the alloys. These results are consistent with the analysis of the kinetic potential polarization curves.

Fig. 7(b) shows the Bode plots of the CoCrFeNiC_x HEAs with different carbon contents. The phase angle of these alloys in the bode plot reaches -80° in the mid-frequency band indicating that these alloys are all able to form a stable passivation film in 3.5% NaCl solution [47]. The Z value of 0.1 Hz is used as the evaluation value of the charge binding ability of the passivation film. Z presents an increasing and then decreasing trend with increasing carbon content. C0.3 alloy has the largest Z value indicating that its passivation film has the strongest charge blocking ability in 3.5% NaCl solution. The addition of appropriate amount of carbon can make the passivation film formed for the alloy with better stability and corrosion resistance.

The structure, strength and the corrosion resistance of the passivation film are analyzed in the form of equivalent circuit fitting. It is evident that the film is mainly capacitive based on the evolution range of the phase angle ($70\text{--}85^\circ$) and the linear slope of the impedance modulus in the middle and low-frequency range (close to -1) in the Bode plot. Based on previous reports [48], The EEC model is shown to be applicable in the impedance analysis of passivation films of carbon doped CoCr-FeMnNi HEAs. Thus, the impedance data were fitted using the equivalent electron circuit (EEC). As depicted in Fig. 7, based on the EEC model, the passive film formed on the HEA surface is considered to have a porous structure and to show non-ideal capacitive behaviour, as shown in Fig. 7. The Nyquist plot in Fig. 7(a) shows that the original data in point shape are in good agreement with the fitted data in line shape, and the fitting coefficient χ^2 is in the order of 1×10^{-4} . This confirms our assumption that the passivation film of present CoCrFeNiC_x HEAs with varying carbon contents is indeed a bilayer structure. The circuit diagram consists of three resistors connected in series and parallel with two ideal capacitor elements, where R_s represents the sum of the solution

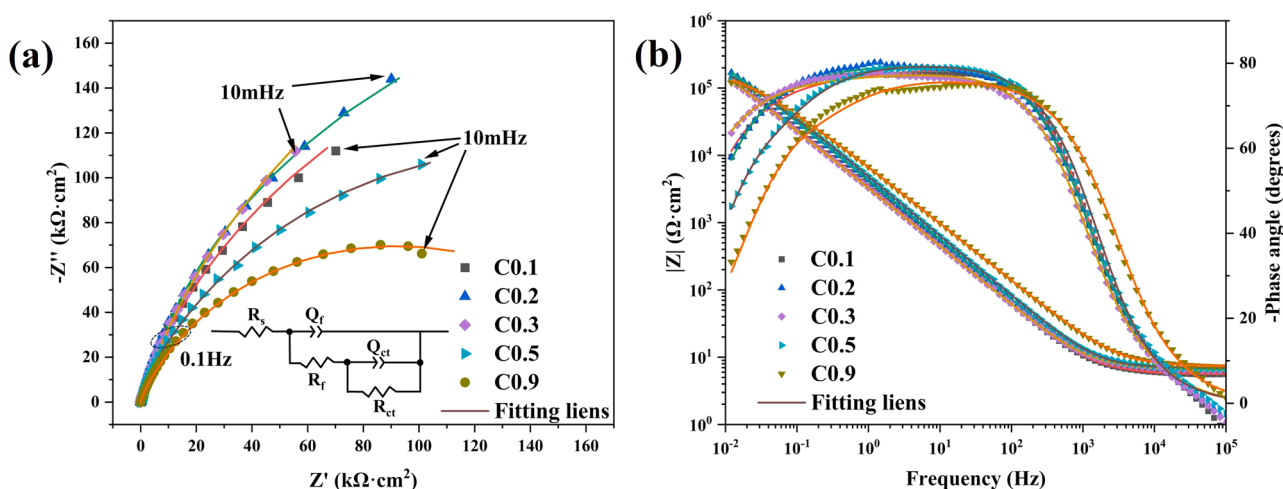


Fig. 7. (a) Nyquist plots and (b) Bode plots of the CoCrFeNiC_x HEAs with different carbon content in 3.5 wt% NaCl solution at room temperature.

resistance and the system external circuit resistance, R_f and Q_f are the passivation film resistance and capacitance with a loose structure on the outside, and R_{ct} and Q_{ct} are the passivation film resistance and capacitance with a dense structure on the inside. To compensate for the inhomogeneities in the system, a constant phase element (CPE) is used to instead of a pure capacitor to characterize the capacitive behavior [47].

The relative fitting parameters are summarized in Table 2. The data in the table show that the resistance R_f of the outer passivation film are all less than the resistance R_{ct} of the inner passivation film. Since the resistance of the passivation film is directly proportional to its corrosion resistance, this result strongly proves that the quality of the passivation film mainly depends on its dense and compact inner layer. The lower value of impedance R_f of the outer passivation film may be due to the high porosity of the outer film, which leads to the electrons can transport through the electrolyte and enter the voids of the passivation film. In addition, the fitting results show that R_{ct} presents a trend of increasing and then decreasing. The C0.3 alloy with the highest R_{ct} value reveals that the passivation film formed in 3.5 % NaCl solution has the best corrosion resistance and the strongest protection for the substrate. This is consistent with the results of the potential polarization curves.

3.4. Corrosion morphology

Fig. 8 shows the corrosion morphology of the HEAs by SEM. The corrosion morphology of the C0.1 alloy [see Fig. 8(a)] shows a large number of shallower corrosion pits on the surface of the alloy. Fig. 8(b) presents the corrosion morphology of the C0.2 alloy, which shows significant intergranular corrosion compared to C0.1 alloy. Fig. 8(c) shows the corrosion morphology of the C0.3 alloy, where the size of the surface pits becomes larger and deeper, and large damage still occurs at the grain boundaries. From the microstructure of the C0.3 alloy, the island-like carbide phases precipitated at the grain boundaries disappeared after the electrochemical corrosion leaving large-sized pits. Fig. 8(d) shows the corrosion morphology of the C0.5 alloy. The corrosion damage is further aggravated compared to the HEAs with lower carbon content. The presence of large corrosion pits on the surface of the alloy indicates that the localized corrosion resistance of the C0.5 alloy in 3.5% NaCl solution is further reduced. This is consistent with the results obtained from the Tafel curves. Moreover, the damage occurs mainly at grain boundaries and is related to the precipitated second phase. The corrosion morphology of the C0.9 alloy displays obvious damage in Fig. 8(e), which can be clearly observed in the local magnified image of the C0.9 alloy [Fig. 8(f)]. This figure shows that corrosion occurs at the phase boundary between the FCC phase and the M₇C₃ phase.

4. Discussion

4.1. Characteristics of passivation film

Numerous studies have shown that the corrosion resistance of the passivation films plays an important role in the corrosion prevention of alloys [49–53]. The constant potential polarisation method to obtain a steady-state passivation film has been widely used to characterise the corrosion resistance of alloys [54–56]. In order to further investigate the effect of different carbon contents on the passivation film properties. EIS

measurements were conducted at applied potentials after film formation for 1 h. The constant potential $i-t$ curves for the C0.1, C0.3, and C0.9 HEAs are presented in Supplementary Fig. S1. The EIS results are depicted in the form of Nyquist plots and Bode plots and shown in Fig. 9, including the fitting results as solid lines.

All the spectra are characterized the same half-arc shape in the Nyquist diagrams, indicating similar passive mechanism of the C0.1, C0.3, and C0.9 HEAs, as shown in Fig. 9(a)-(c). The film formation potential has a considerable effect on the EIS of the HEAs in the 3.5 wt% NaCl solution. The impedance of the system gradually increases as the film-forming potential moves in the positive direction. This indicates that the corrosion resistance of the passivation films formed on the surface of these HEAs is increasing with the positive shift of the polarization voltage. Fig. 9(d)-(e) show that the phase angle in the Bode plot can reach -80° in the mid-frequency band, which implies that the stable passivation films at different polarization voltages can be formed for the three alloys. We still apply the equivalent circuit fitting form to analyze the structure of the passivation film and evaluate the passivation film corrosion resistance. The specific parameters obtained are summarized in Table 3.

The film thickness is a significant factor that affects the barrier properties of its passive layer. The data on capacitance presented in Table 3 can be used to estimate the thickness of the passive film. This is highly significant to understand the barrier properties of the films. The film passivation thickness (L_{ss}) can be calculated by the following equation [31,57]:

$$C_{\text{eff}} = \frac{\epsilon \epsilon_0 A}{L_{ss}} \quad (1)$$

where C_{eff} is the effective capacitance of the passivation film, ϵ is the dielectric constant (12) [43,48], ϵ_0 is the vacuum permittivity ($8.8542 \times 10^{-12} \text{ F m}^{-1}$), and A is the effective surface area of the sample. According to Wallinder et al. [42] results, the effective area is two times of the geometric area if a roughness factor is assumed as 2. The effective capacitance (C_{eff}) of the passivation film is closely related to the parameter (Q) of the CPE element. Orazem et al. [58] compared the four commonly used approaches to obtain the C_{eff} of a system from the predicted CPE parameters. Among them, the expression proposed by Brug et al. [59] gives reasonable results. In the current work, the thickness of the film calculated using the expression proposed by Brug et al. is greater than 7 nm [see Supplementary Table S1], which is much higher than the reported value (1–3 nm) [26,60,61]. Therefore the power law distribution proposed by HirsChorn et al. [62] was chosen to calculate the C_{eff} value for the present HEAs [63,64]:

$$C_{\text{eff}} = g Q (\rho_d \epsilon \epsilon_0)^{1-n} \quad (2)$$

In Eq. (2), the parameter ρ_d is the resistivity which can be assigned a value of $500 \Omega \text{cm}^2$, g is a function of n and can be expressed by the following equation [62]:

$$g = 1 + 2.88(1 - n)^{2.375} \quad (3)$$

where n value is the ratio of ideal capacitance to actual capacitance. Then, combining Eqs. (1)-(3), the film thickness can be calculated using the following relation [60,63,64]:

Table 2

Equivalent electron circuit parameters of the electrochemical impedance spectroscopy data of the CoCrFeNiC_x HEAs with different carbon content in the 3.5 wt% NaCl at room temperature.

Alloys	$R_s (\Omega \text{ cm}^2)$	$R_f (\Omega \text{ cm}^2)$	$R_{ct} (10^5 \Omega \text{ cm}^2)$	$Q_f (\Omega^{-1} \text{cm}^{-2} \text{s}^n)$	n_f	$Q_{ct} (\Omega^{-1} \text{cm}^{-2} \text{s}^n)$	n_{ct}	χ^2
C0.1	5.66	4.14	4.61	1.22×10^{-5}	1.000	4.76×10^{-5}	0.813	9.805×10^{-4}
C0.2	6.79	82.44	4.76	1.91×10^{-5}	0.946	2.83×10^{-5}	0.826	4.776×10^{-4}
C0.3	6.45	3.79	6.13	1.65×10^{-5}	0.956	4.82×10^{-5}	0.813	5.721×10^{-4}
C0.5	6.92	135,700	1.46	3.99×10^{-5}	0.888	3.43×10^{-5}	0.854	5.341×10^{-4}
C0.9	7.36	75,460	1.06	3.02×10^{-5}	0.851	1.68×10^{-5}	0.810	6.291×10^{-4}

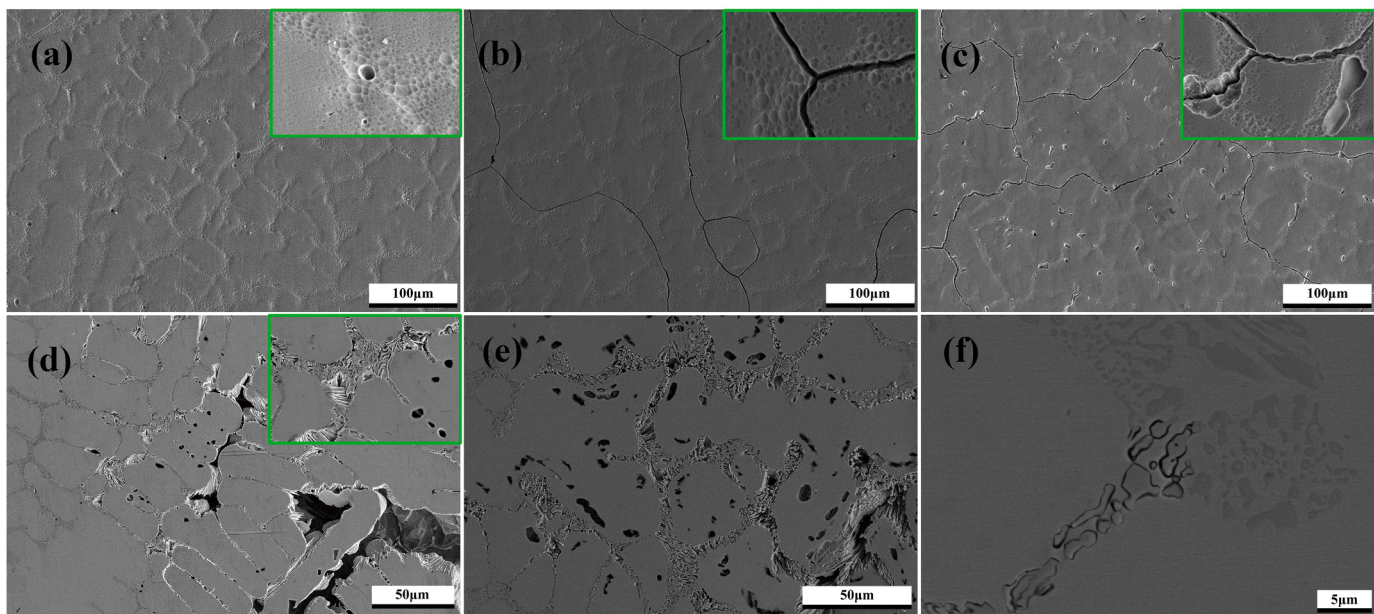


Fig. 8. Surface morphologies of C0.1 (a), C0.2 (b), C0.3 (c), C0.5 (d), and C0.9 (e) HEAs after the potentiodynamic polarization tests in 3.5 wt% NaCl solution. (f) is local magnified of (e).

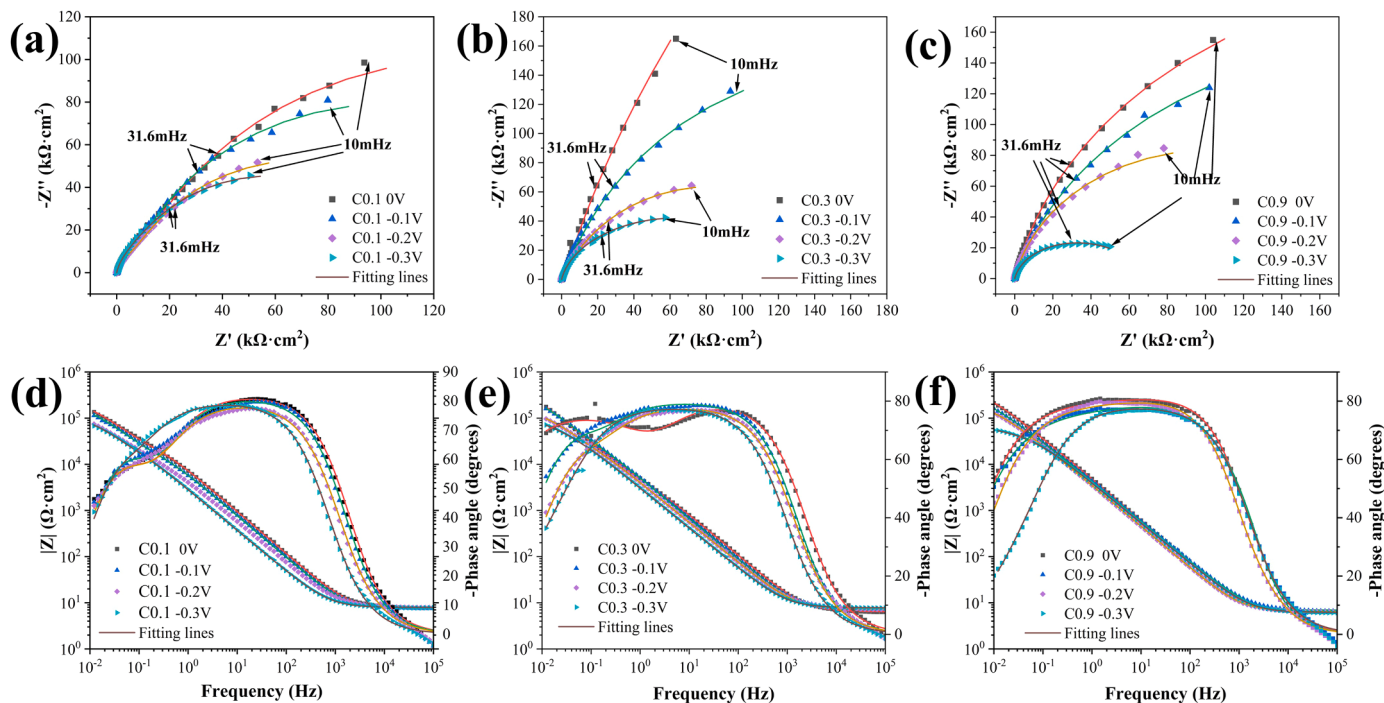


Fig. 9. Nyquist and Bode plots of C0.1 (a, d), C0.3 (b, e), C0.9 (c, f) HEAs.

$$L_{ss} = \frac{(\epsilon e_0)^n A}{g Q \rho_d} \quad (4)$$

The film thickness as well as its dependence on the film formation potential is shown in Fig. 10. The film thickness is in the range of 0.5–2.5 nm, which is consistent with literatures. The linear relationship between L_{ss} and E can deduce the film formation ratio (r) and the average field strength (E_0) of the passivation film according to the following expression [65]:

$$L_{ss} = rE + B = \frac{1}{E_0}(1 - \alpha)E + B \quad (5)$$

where α is the polarizability of the film/solution interface, B is a constant. With value of α as 0.7, the film formation rate versus the electric field strength of the passivated film is summarized in the table of Fig. 10. The film formation ratios for the three alloys between 2 and 4 nm/V and decreased with the increase of the carbon content, which proves that the incorporation of carbon atoms has a hindering effect on the passivation film formation.

The calculated values of E_0 are shown in the table of Fig. 10. Note that the E_0 values obtained are approximately 1 MV/cm, which is similar to the reported value of stainless steel [66]. The results indicate

Table 3

Equivalent electron circuit parameters of the electrochemical impedance spectroscopy data of C0.1, C0.3, and C0.9 HEAs in the 3.5 wt% NaCl solution at room temperature.

Alloys	Applied potential(V _{sce})	R _s ($\Omega \text{ cm}^2$)	R _f ($\Omega \text{ cm}^2$)	R _{ct} ($\Omega \text{ cm}^2$)	Q _f ($\Omega^{-1} \text{cm}^{-2} \text{s}^n$)	n _f	Q _{ct} ($\Omega^{-1} \text{cm}^{-2} \text{s}^n$)	n _{ct}	χ^2
C0.1	0	7.86	3.71×10^4	2.24×10^5	2.40×10^{-5}	0.914	3.42×10^{-5}	0.831	9.49×10^{-4}
	-0.1	7.67	3.00×10^4	1.69×10^5	3.06×10^{-5}	0.906	3.77×10^{-5}	0.861	1.02×10^{-3}
	-0.2	7.98	2.34×10^4	1.15×10^5	4.51×10^{-5}	0.886	5.81×10^{-5}	0.842	6.59×10^{-4}
	-0.3	7.91	4.50×10^4	6.8×10^4	6.93×10^{-5}	0.889	6.90×10^{-5}	0.892	6.61×10^{-4}
C0.3	0	6.41	8.14×10^3	1.68×10^6	3.03×10^{-5}	0.891	1.96×10^{-5}	0.790	8.20×10^{-4}
	-0.1	7.51	8.46×10^4	2.80×10^5	3.80×10^{-5}	0.888	1.78×10^{-5}	0.874	4.90×10^{-4}
	-0.2	7.36	5.29×10^4	1.11×10^5	4.91×10^{-5}	0.872	3.25×10^{-5}	0.822	4.07×10^{-4}
	-0.3	7.80	7.56×10^4	4.80×10^4	6.06×10^{-5}	0.870	1.63×10^{-4}	0.743	6.53×10^{-4}
C0.9	0	6.33	9.84	4.92×10^5	1.44×10^{-5}	0.985	2.71×10^{-5}	0.817	1.06×10^{-3}
	-0.1	6.96	48.67	4.08×10^5	1.56×10^{-5}	0.986	3.42×10^{-5}	0.767	2.22×10^{-3}
	-0.2	6.47	7.63	2.23×10^5	1.75×10^{-5}	0.987	4.11×10^{-5}	0.813	1.04×10^{-3}
	-0.3	6.20	47,520	2.00×10^4	5.05×10^{-5}	0.873	2.22×10^{-4}	0.740	5.50×10^{-4}

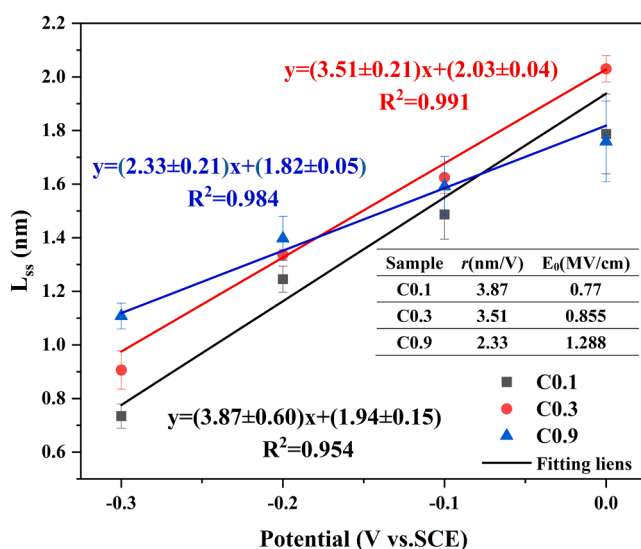


Fig. 10. Calculated passive film thickness of the C0.1, C0.3, and C0.9 HEAs in the 3.5 wt% NaCl solution, and the fitting parameters are shown in the insets of the figure.

that the electric field strength of the passivation film increases with the increase of carbon content. The electric field strength is directly proportional to the resistance. So a passivation film with a high electric field strength implies a higher resistance, which prevents the current from flowing through the metal surface and reduces the electrochemical reaction of the metal. This proves that the addition of carbon atoms increases the ability of the passivation film to block electron transport and hence inhibits corrosion.

4.2. Mott-Schottky analysis

Electrochemical capacitance of the passive film/electrolyte interface is recorded as a function of the applied potential to characterize the semiconductive property and the density of charge carriers for the passive film. According to the Mott-Schottky theory, the space charge capacitance for a semiconductor electrode under the depletion condition can be given by the following equations [67,68]:

$$\frac{1}{C_{SC}^2} = \frac{2}{\epsilon \epsilon_0 e N_D} \left(E - E_{FB} - \frac{KT}{e} \right) \text{n-type} \quad (6)$$

$$\frac{1}{C_{SC}^2} = \frac{2}{\epsilon \epsilon_0 e N_A} \left(E - E_{FB} - \frac{KT}{e} \right) \text{p-type} \quad (7)$$

where N_D and N_A are the densities of the donor and acceptor,

respectively, e is the electron charge (1.6×10^{-19} C), E is the applied potential, E_{FB} is the flat charged potential, K is the Boltzmann constant (1.38×10^{-23} J/K), T is the absolute temperature (K). ϵ and ϵ_0 have the same meaning as before. The above equation show that the curve of C_{SC}^{-2} versus E should be a straight line whose slope is inversely proportional to the doping concentration.

Fig. 11(a)-(c) shows the Mott-Schottky plots for the passive film formed on C0.1, C0.3, and C0.9 HEAs at different anodic potentials for 1 h in 3.5% NaCl solution. Upon close examination, it is easily revealed that there is a linear relationship between C^{-2} and E in the high potential domain. The positive slope indicates the n-type semi-conducting nature of the passivation film, suggesting the presence of a large number of oxygen vacancies and/or cation-filled gaps. The variation of the slopes in this region with applied potential may be linked to the changes of the passivation film structure and composition. The donor density (N_D) of the passivated film can be calculated from the slope of the linear part in the Mott-Schottky plots according to Eq. (6). The fitted values of the passivation films for the C0.1, C0.3, and C0.9 alloys are given in Fig. 11 (d-f). The decrease in N_D values with increasing formation potential is usually attributed to the fact that passivation films formed at low action potentials have more disordered structures and higher defect densities than those formed at high action potentials [69]. Furthermore, this result is consistent with the trend of increasing film resistance with increasing polarization potential. According to the point defect model (PDM) [70] the following theoretical relationship exists between N_D and E :

$$N_D = \omega_1 \exp(-bE) + \omega_2 \quad (8)$$

where ω_1 , ω_2 , and b are constants. The exponential fitting curves to the experimental results are also shown in Fig. 11(d)-(f) and the fitting parameters are listed in Table 4. These parameters are related to defect diffusion within the passive film. Combining the parameters in Table 4, the diffusion coefficient (D_0) of a point defect in a passivated film can be obtained using the Nernst-Plank transport equation [70]:

$$D_0 = \frac{I_{ss}RT}{4eF\omega_2 E_0} \quad (9)$$

where I_{ss} is the average current density of the steady-state passivation film and the measured current flow is mainly due to the flux of oxygen vacancies as predicted by PDM [71]. F is the Faraday constant (96,494 C/mol), R is the gas constant ($8.314 \text{ J mol}^{-1}\text{K}^{-1}$). The average values of the steady-state passivation film current densities (I_{ss}) and ω_2 for the HEAs are listed in Table 4. These values of E_0 are already obtained in the insets in Fig. 10. Therefore, the diffusion coefficient D_0 of the point defects (mainly oxygen vacancies in this study) can be calculated according to Eq. (9). The results of the values are summarized in Table 4.

It is noteworthy that the D_0 values of the passivation films of C0.1, C0.3 and C0.9 alloys in 3.5% NaCl solution are in the order of 10^{-17}

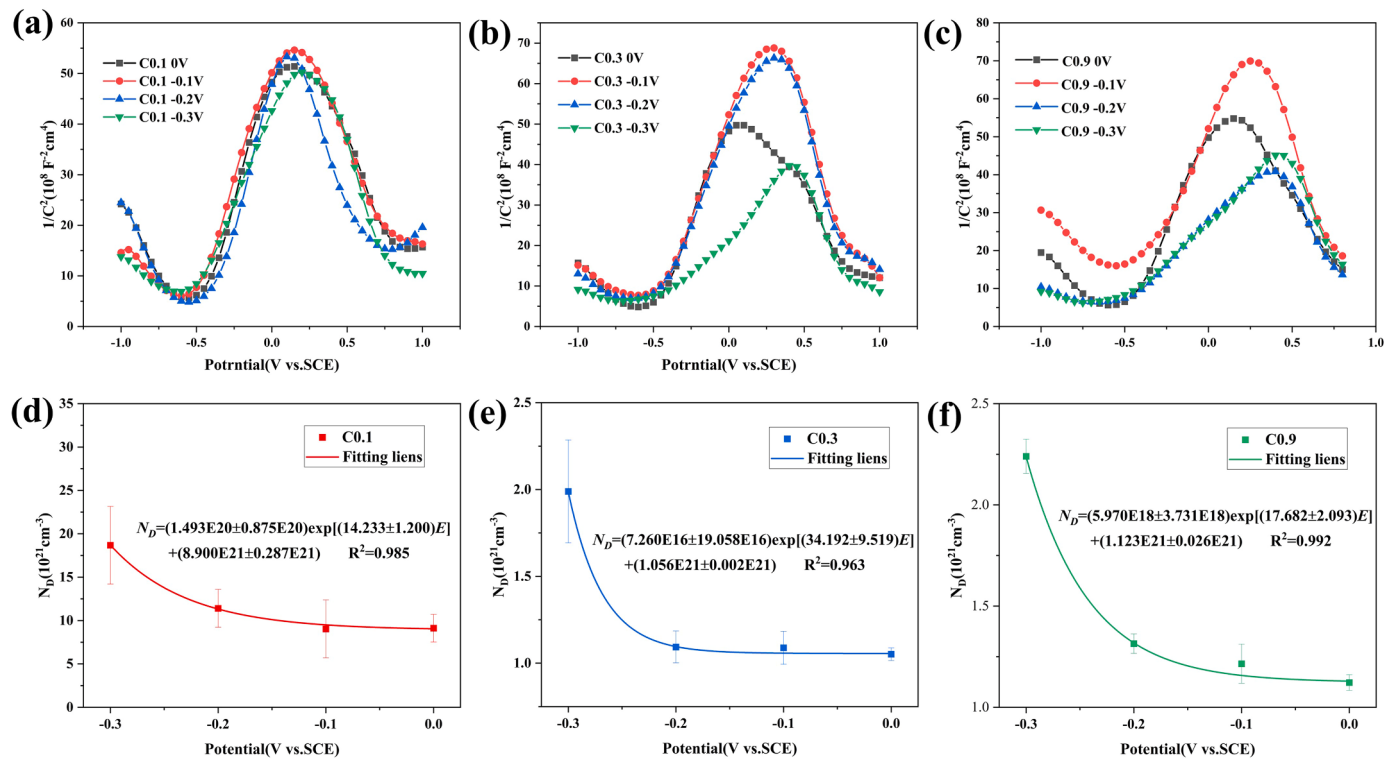


Fig. 11. Mott-Schottky plots for the passive film formed on C0.1 (a), C0.3 (b), and C0.9 (c) HEAs at different anodic potentials for 1 h in 3.5 wt% NaCl solution. The derived experimental data of donor densities versus anodic potentials and their fitting lines for the three alloys (d-f).

Table 4

Fitting parameters for the line fitting the data of donor density to anodic potential, steady-state current density and diffusivity of the passivated films for the C0.1, C0.3 and C0.9 alloys.

Sample	ω_1	ω_2	b	R^2	$I_{ss}(\text{Acm}^{-2})$	$D_0(\text{cm}^2\text{s}^{-1})$
C0.1	$1.493 \times 10^{20} \pm 10^{21}$	$8.900 \times 10^{21} \pm 1.200$	14.233	0.985	4.50×10^{-7}	4.082×10^{-18}
C0.3	$7.260 \times 10^{16} \pm 10^{21}$	$1.056 \times 10^{21} \pm 9.519$	34.192	0.963	2.60×10^{-7}	1.301×10^{-17}
C0.9	$5.970 \times 10^{18} \pm 10^{21}$	$1.123 \times 10^{21} \pm 2.093$	17.682	0.992	4.82×10^{-7}	3.165×10^{-17}

cm^2s^{-1} . It is worth noting that the D_0 values of the passivation films of the three alloys differ from the values estimated between 10^{-16} and $10^{-14} \text{ cm}^2\text{s}^{-1}$ [72]. This may be attributed to two possible reasons, i.e., one is that the solid-state diffusion process can lead to the low diffusion coefficients, which are exacerbated by the addition of alloying carbon elements. Another is that the diffusion coefficient within the passivated film depends strongly on the experimental conditions, the calculation formula, the passivation time, and the electrolyte. Therefore, there is a slight deviation between the D_0 values calculated in this article and those in other literatures. D_0 of point defects is a key parameter in describing the migration of point defects and the kinetics of film growth [72]. The D_0 values of the current alloy passivation films show an increasing trend with higher carbon content, reflecting the influence of the alloy composition on the passivation kinetics to some extent. The passivation film of C0.9 alloy has the highest oxygen vacancy diffusion coefficient, which means it has higher flux and higher film formation rate [71]. In addition, higher diffusion coefficients allow the dynamic

competition between dissolution and growth of the passivation films to be equilibrated at higher current levels. The relatively higher passivation current density I_{pass} observed for C0.9 alloy in the polarization curves (shown in Table 1) may be related to the higher D_0 values. However, high I_{pass} values mean that the passivation film is not dense, which is detrimental to corrosion resistance.

4.3. XPS analysis

Alloy corrosion resistance depends largely on the composition of the passivation film in a certain corrosive environment [73,74]. XPS technology was used to initially examine the chemical composition and valence of the passivation film to clarify the influence of carbon on the composition of the alloy passivation film and to reveal the reasons for the evolution of the present alloy's corrosion resistance. The calibration of the peak positions was performed with reference to C1s (284.80 eV). Fig. 12 shows the photoelectron peaks of Co 2p/2, Cr 2p3/2, Fe 2p3/2, Ni 2p3/2, and O1s obtained from the passivation films formed on C0.1, C0.3, and C0.9 HEAs after 1 h of polarization at 0 V. These peaks are fitted using Avantage software and the results of the fitting curves are shown as colored lines in Fig. 12.

All the constituent elements of these HEAs are detected by the XPS tests. From the macroscopic point of view, the peak patterns of the elements change significantly with the increase of carbon content indicating that carbon content has a greater effect on the composition of the passivation film. Co 2p3/2 peaks at 778.1 eV, 780.3 eV, 782.4 eV, 586.1 eV are suitable for the metals Co^0 , Co^{2+} , Co^{3+} , and $\text{Co}_{\text{sat}}^{2+}$, respectively. Cr 2p3/2 peaks at 573.7 eV, 576.3 eV, 577.1 eV are suitable for the metals Cr^0 , Cr_2O_3 , and $\text{Cr}(\text{OH})_3$, respectively. The Fe 2p3/2 peaks are categorized into Fe^0 (706.9 eV), $\text{Fe}_{\text{ox}}^{2+}$ (708.4 eV), $\text{Fe}_{\text{ox}}^{3+}$ (710.0 eV) $\text{Fe}_{\text{hy}}^{3+}$ (711.8 eV), and FeOOH (714.9 eV). The spectra of Ni 2p3/2 at 852.6 eV, 854.7 eV, and 856.2 eV are fitted to three peaks for the metal Ni^0 , $\text{Ni}_{\text{ox}}^{2+}$ and $\text{Ni}_{\text{hy}}^{2+}$ [75]. In addition, three different substances, O^{2-} (529.8 eV), OH^- (531.4 eV) and H_2O (533.0 eV), are found in the O 1s spectra of the passivation film. The findings of O^{2-}

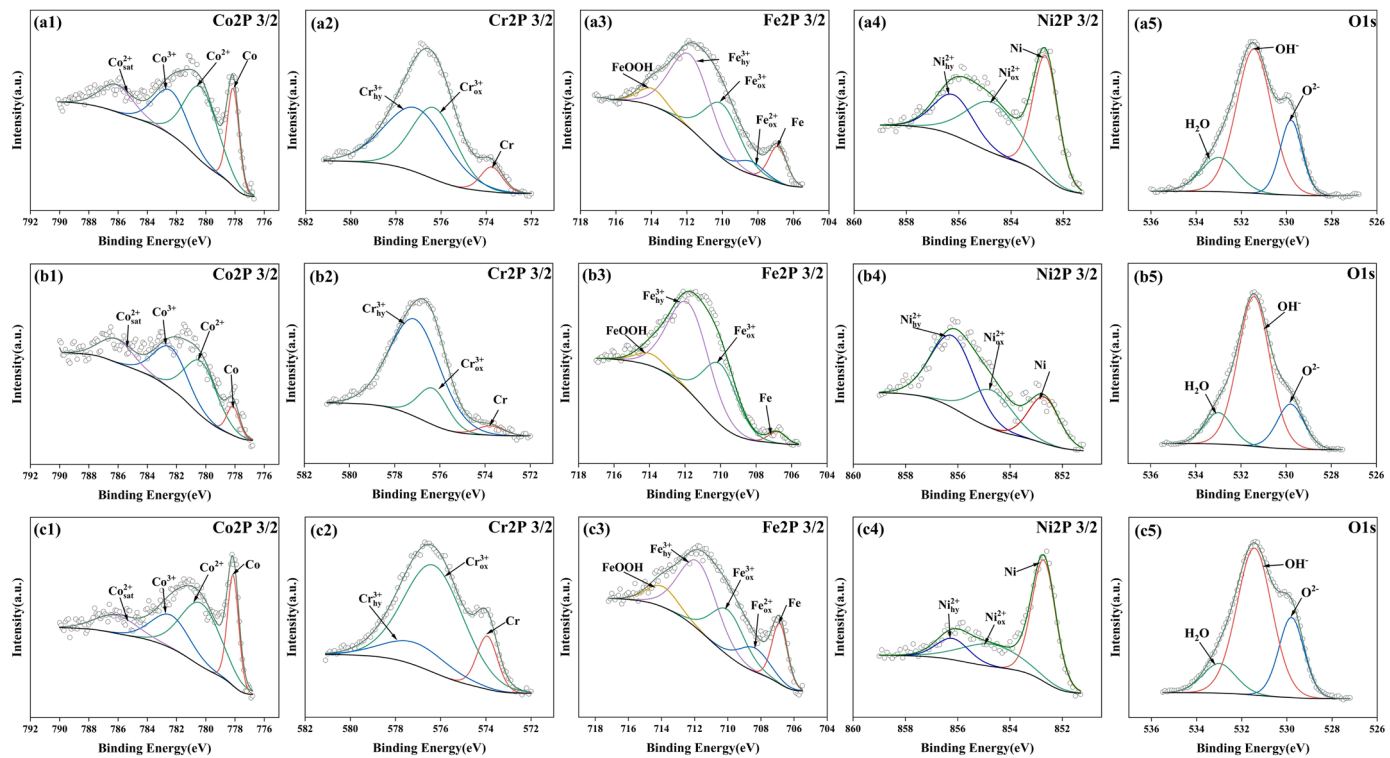


Fig. 12. Photoelectron spectra of various elements in the steady-state passivation films of C0.1, C0.3 and C0.9 alloys.

(529.8 eV), OH⁻ (531.4 eV) are related to the metal oxides and hydroxides in the passivation film [76], and the H₂O may be the bound water in the passivation film [77]. These results show that the oxides and hydroxide compounds of the alloy composition elements are the main components of the passivation film.

To investigate the composition difference of the passive films formed on the three alloys, the atomic percentages of the composition peaks to the total intensity of the Co 2p3/2, Cr 2p3/2, Fe 2p3/2, Ni 2p3/2, and O1s spectra are presented in Fig. 13. From Fig. 13(a), it can be seen that the contents of metal monomers all present a decreasing and then increasing trend with the increase of carbon content. It is well known that the passivation film mainly consists of oxides and hydroxides of metal elements, so that the signal of metal monomers mainly comes from the substrate. This means that the thickness of the passivation film presents an increasing and then decreasing trend with the increase of

carbon content. The reason for this may be that the increase in carbon content in the passivation film of C0.3 alloys inhibits the dissolution of the corrosion resistant elements, which leads to a thickening of the passivation film. The optimization of the passivate film thickness is beneficial to the improvement of the corrosion resistance of the alloy. Depending on the analysis of the passivate film properties, we found that the results of the EIS data measured under 0 V show that the thickness (L_{ss}) of the passivate film is larger for C0.3 alloy than that for the other two alloys. The results of the EIS data analysis are consistent with the XPS analysis results. The photoelectron spectra of O1s with different carbon contents show that the main components of the passivation films are metal hydroxides. According to the two-layer film theory [78,79] for the actual passivation film structure, the inner layer consists of dense metal oxides, while the loose outer passivation film is mainly composed of hydroxides. This may be the main reason for the significant increase

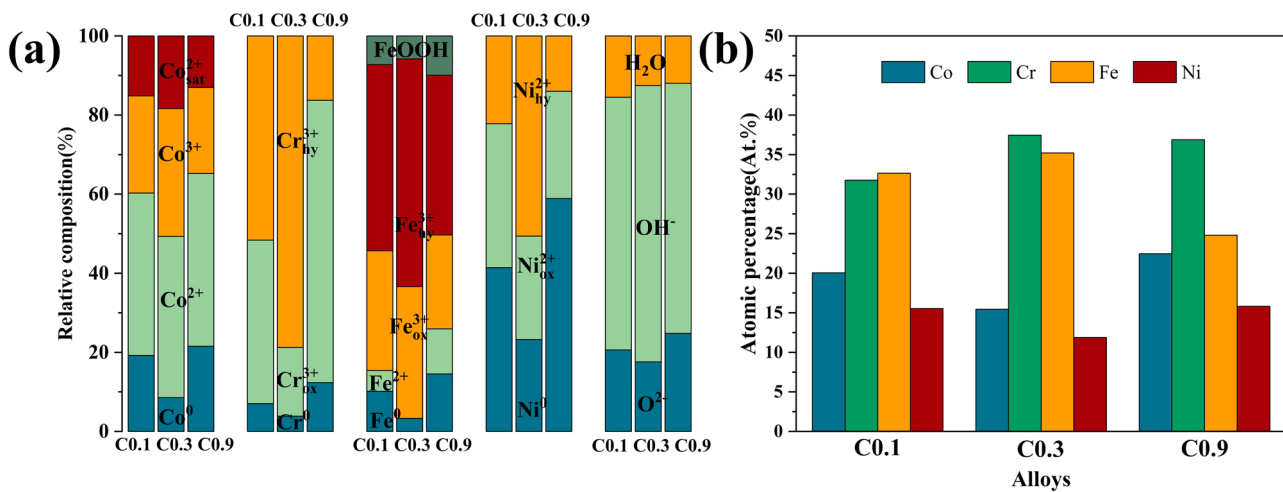


Fig. 13. Valence(a) and content (b) diagrams of various elements in the formation of the passivation films on C0.1, C0.3, and C0.9 alloys.

in the hydroxide content in the passivation film composition. From Fig. 13(b), it can be found that the C0.3 alloy has the highest content of chromium. As the main corrosion-resistant element [80], the higher content of chromium in the passivation film is conducive to improving the corrosion resistance of the alloy. C0.3 alloys have the strongest corrosion resistance probably due to the increase of corrosion resistant elements in the passivation film. In addition, we observed that the main form of Cr atoms present in the C0.9 alloy is Cr_2O_3 , probably due to the sparse or thin outer passivation film, with most of the XPS signal coming from the inner dense passivation film. In the study of the formation of passivation film in the Cl^- environment of stainless steel [78], the passivation film is composed of a Cr-rich and Fe-poor inner passivation film and a Fe-rich and Cr-poor outer passivation film. The properties of the stainless steel are very similar to the present alloy. The significant decrease in the Fe content of the C0.9 alloy is attributed to the loosening or thinning of the Fe-rich outer passivation film, which is corroborated by the fact that the impedance of the outer passivation film is very much lower than that of the inner passivation film based on the EIS results. The Cr in the C0.9 alloy is concentrated in the M_7C_3 phase, and the reduction of Cr in the matrix leads to a decrease in the corrosion resistance of the matrix.

4.4. Corrosion mechanisms

The HEAs containing different carbon content show different corrosion mechanisms. For the C0.1 HEA, the observed corrosion morphology without steady state pitting pits indicates that the uniform corrosion occurs on this alloy. The grain boundary corrosion appears on the C0.2 and C0.3 alloys surface, which may be due to the oversaturated solid solution of carbon atoms aggregating at grain boundaries, resulting in a decrease in grain boundary energy and corrosion resistance. However, for the C0.5 and C0.9 alloys, the obvious corrosion pits can be observed around the M_7C_3 carbides. The formation and coarsening of carbides change the corrosion mechanism and greatly reduce the corrosion resistance of the HEAs. Next, we conducted an in-depth analysis of the impact of carbides precipitation on the corrosion mechanism of the present HEAs.

Elemental distribution and phase composition decisions are the key factors in determining the corrosion resistance of the ensemble [81]. SKPFM was used to characterize the morphology, surface potential maps and potential profiles of the C0.9 alloy and to assess the anodic and cathodic interactions during the corrosion process. Fig. 14 shows the results of AFM scanning of the C0.9 HEA. The dark yellow FCC matrix phase and the bright white M_7C_3 phase can be observed in Fig. 14(a), which agrees well with the SEM results. Fig. 14(b) shows the potential difference between the two phases. The potential data along the white line in Fig. 14(b) is present in Fig. 14(c). As seen in Fig. 14(c), the second M_7C_3 phase has a lower potential than the FCC matrix phase. This means

that the two phases will undergo galvanic coupled corrosion in the electrolyte solution, and the FCC matrix phase with higher positive potential will act as the anode in the galvanic corrosion. During the electrochemical corrosion process, the anode is oxidized, which is reflected in the destruction of the FCC phase.

In conventional alloy corrosion, pitting goes through a sub-stable growth phase before stabilizing [82]. Substable pitting tends to develop in weak areas of the passivation film, such as surface defects, phase interfaces, or chromium depleted areas. During sub-stable pitting growth, anions like Cl^- and OH^- accumulate in the pitting area to neutralize metal cations dissolved from the passivate film. Hydroxidation of the metal cations leads to localised acidification, promoting sub-stable pitting growth. If diffusive dilution of local anions and H^+ is not enough to continue dissolving the metal, repassivation occurs. Additionally, the depth of the pitting pit itself acts as a diffusion barrier to maintain continued metal dissolution. In the early stages of pitting growth, the pit's depth may be insufficient for stable growth, requiring coverage with porous corrosion products as an additional ion diffusion barrier. As the pitting depth increases, it becomes an independent diffusion barrier, transitioning from sub-stable pitting to steady-state pitting.

In order to clearly demonstrate the corrosion mechanism of the HEAs containing carbides. With increasing carbon content, C0.3 HEA formed island-like precipitates at grain boundaries. In addition to this, the grain boundaries were enriched with carbon atoms or tiny carbides, which caused galvanic coupling corrosion and intergranular corrosion on the surface of C0.3 HEA. Fig. 15 shows the schematic diagrams of corrosion mechanisms for C0.3 and C0.9 HEAs. Due to the galvanic coupling corrosion between the FCC phase and the M_7C_3 carbides, a corrosion crater formed on the FCC phase region extends along the M_7C_3 phase towards the interior of the alloy, as shown in Fig. 15(b) and (e). Fig. 15(c) and (f) show that the corrosion rate is accelerated when the corrosion pits formed by galvanic corrosion reaches a certain depth. This is due to the fact that the corrosion pits block the migration of the metal oxygen ions. The enrichment of metal cations at the depth of the pits leads to solution acidification by the release of H^+ from the water solution, which together with the Cl^- in the solution leads to the intensification corrosion of the alloy.

5. Conclusions

The effect of carbon content on the microstructure and corrosion resistance of CoCrFeNi HEA was investigated by SEM, TEM, SKPFM, TAFEL, EIS, M-S, CPP and XPS tests. The main conclusions are summarized as follows:

- 1) The phase structures of the CoCrFeNi_x ($x = 0.1, 0.2, 0.3, 0.5$, and 0.9 , wt%) HEAs change from single FCC phase ($x = 0.1, 0.2$, wt%) to FCC+ M_7C_3 phases ($x = 0.3, 0.5$, and 0.9 , wt%) with increasing the

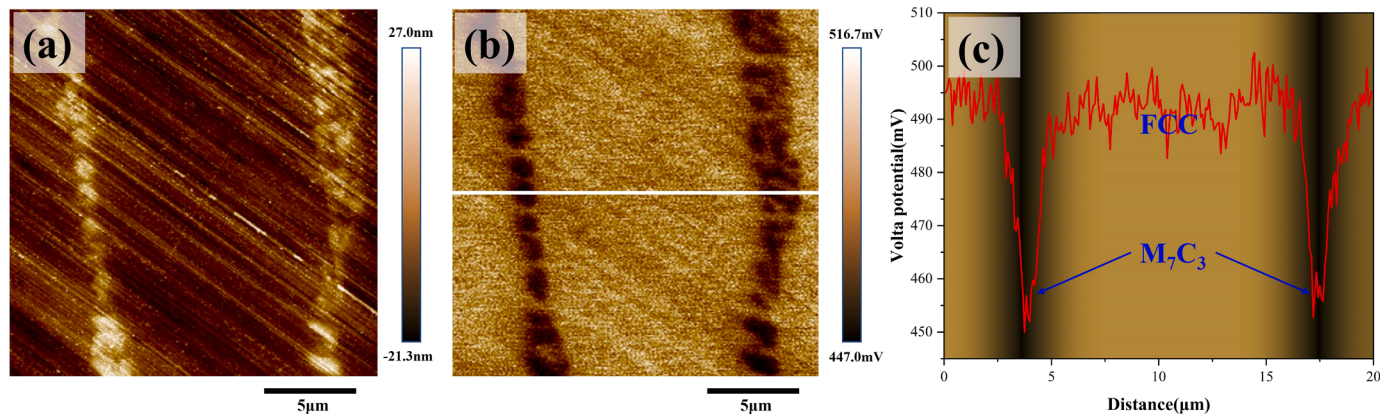


Fig. 14. (a) Microstructure of the C0.9 HEA; (b) V_{CPD} pattern; (c) Potential line profile.

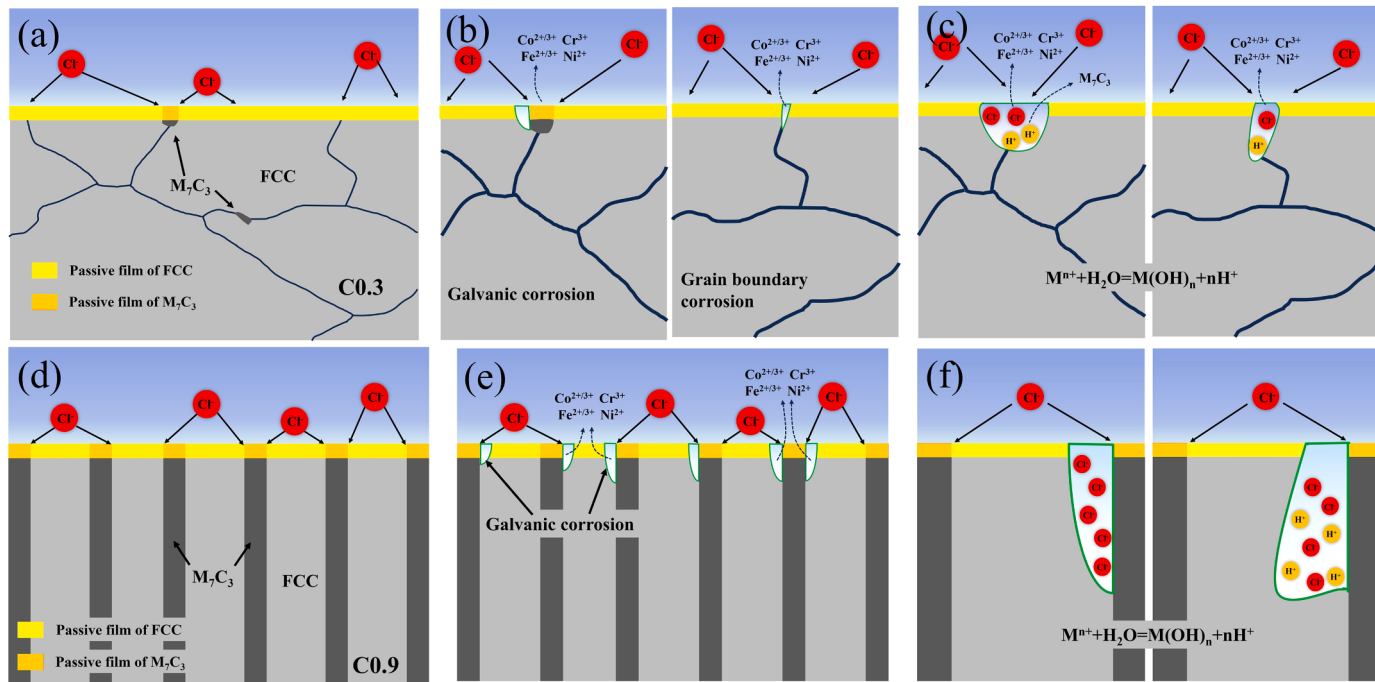


Fig. 15. Corrosion mechanism diagram for Co0.3 and Co0.9 HEAs.

carbon content. The orientation relationship between the M₇C₃ precipitated phase and the FCC matrix is (020)_{FCC}//(011-0)_{M7C3} and [001]_{FCC}//[21-1-0]_{M7C3}.

2) Based on the impedance spectra and potential polarization curves, the corrosion resistance of the CoCrFeNiC_x HEAs present a tendency of enhancing and then weakening. The Co0.3 alloy with the largest impedance and the smallest dissolution rate of the passivation film has the best corrosion resistance in 3.5% NaCl solution. Microstructural observations after potentiodynamic polarisation tests show that the low carbon content FCC single phase alloy (Co0.1) exhibits homogeneous corrosion; the medium carbon content alloys (Co0.2, Co0.3) exhibit intergranular corrosion; and the alloys with pronounced carbide precipitation (Co0.5, Co0.9) undergo galvanic coupling corrosion, which occurs along the FCC side of the M₇C₃ phase, and this is confirmed by the SKPFM measurements.

3) The EIS and M-S results after constant potential polarisation showed that the electric field strength (E_0) oxygen vacancy diffusion coefficient (D_0) of the passivated film and increased with the increase of carbon content, with the maximum values of 1.288×10^6 Vcm⁻¹ and 3.165×10^{-17} cm²s⁻¹, respectively, which together resulted in the optimum corrosion resistance of Co0.3 HEA.

4) XPS results show that the increase of carbon content inhibits the dissolution of corrosion resistant elements in the passivate film resulting in a change in the thickness of the passivate film. A large number of chromium-rich carbides in Co0.9 HEA lead to a decrease in the corrosion resistance of the alloy. The optimization of passivate film thickness and the addition of corrosion-resistant elements are the main reasons for improving the corrosion resistance of Co0.3 HEA.

CRediT authorship contribution statement

Qixiang Jia: Formal analysis, Data curation, Conceptualization. **Lijun Zhang:** Formal analysis, Data curation, Conceptualization. **Xueming Wei:** Writing – original draft, Methodology, Investigation, Formal analysis, Conceptualization. **Chunzhi Zhang:** Formal analysis, Data curation, Conceptualization. **Fengyi Zhang:** Investigation, Formal analysis. **Gong Li:** Supervision, Conceptualization. **Hui Jiang:** Formal analysis, Data curation, Conceptualization. **Dongtao Duan:** Formal

analysis, Data curation, Conceptualization. **Kai Sun:** Formal analysis, Data curation, Conceptualization.

Declaration of Competing Interest

The authors declare that they have no known competing financial interests or personal relationships that could have appeared to influence the work reported in this paper.

Data availability

No data was used for the research described in the article.

Acknowledgments

This work was supported by the National Natural Science Foundation of China (52204373).

Appendix A. Supporting information

Supplementary data associated with this article can be found in the online version at doi:10.1016/j.corsci.2024.111965.

References

- [1] J.W. Yeh, S.K. Chen, S.J. Lin, J.Y. Gan, T.S. Chin, T.T. Shun, C.H. Tsau, S.Y. Chang, Nanostructured high-entropy alloys with multiple principal elements: novel alloy design concepts and outcomes, *Adv. Eng. Mater.* 6 (2004) 299–303, <https://doi.org/10.1002/adem.200300567>.
- [2] Y. Shi, L. Collins, N. Balke, P.K. Liaw, B. Yang, In-situ electrochemical-AFM study of localized corrosion of Al CoCrFeNi high-entropy alloys in chloride solution, *Appl. Surf. Sci.* 439 (2018) 533–544, <https://doi.org/10.1016/j.apsusc.2018.01.047>.
- [3] D.L. Beke, G. Erdélyi, On the diffusion in high-entropy alloys, *Mater. Lett.* 164 (2016) 111–113, <https://doi.org/10.1016/j.matlet.2015.09.028>.
- [4] K.Y. Tsai, M.H. Tsai, J.W. Yeh, Sluggish diffusion in CoCrFeMnNi high-entropy alloys, *Acta Mater.* 61 (2013) 4887–4897, <https://doi.org/10.1016/j.actamat.2013.04.058>.
- [5] J. Yeh, S. Chang, Y. Hong, S. Chen, S. Lin, Anomalous decrease in X-ray diffraction intensities of CuNiAlCoCrFeSi alloy systems with multi-principal elements, *Mater. Chem. Phys.* 103 (2007) 41–46, <https://doi.org/10.1016/j.matchemphys.2007.01.003>.

- [6] J. Yeh, S. Lin, T. Chin, J. Gan, S. Chen, T. Shun, C. Tsau, S. Chou, Formation of simple crystal structures in CuCoNiCrAlFeTiV alloys with multiprincipal metallic elements, *Mater. Sci. Eng. A* 35 (2004) 2533–2536, <https://doi.org/10.1007/s11661-006-0234-4>.
- [7] Y. Zhang, T.T. Zuo, Z. Tang, M.C. Gao, K.A. Dahmen, P.K. Liaw, Z.P. Lu, Microstructures and properties of high-entropy alloys, *Prog. Mater. Sci.* 61 (2014) 1–93, <https://doi.org/10.1016/j.pmatsci.2013.10.001>.
- [8] L.J. Santodonato, Y. Zhang, M. Feygenson, C.M. Parish, M.C. Gao, R.J.K. Weber, J. C. Neufeind, Z. Tang, P.K. Liaw, Deviation from high-entropy configurations in the atomic distributions of a multi-principal-element alloy, *Nat. Commun.* 6 (2015) 5964, <https://doi.org/10.1038/ncomms6964>.
- [9] J.-W. Yeh, S.-J. Lin, T.-S. Chin, J.-Y. Gan, S.-K. Chen, T.-T. Shun, C.-H. Tsau, S.-Y. Chou, Formation of simple crystal structures in Cu-Co-Ni-Cr-Al-Fe-Ti-V alloys with multiprincipal metallic elements, *Met. Mater. Trans. A* 35 (2004) 2533–2536, <https://doi.org/10.1007/s11661-006-0234-4>.
- [10] J. Yeh, Overview of high-entropy alloys, in: M.C. Gao, J. Yeh, P.K. Liaw, Y. Zhang (Eds.), *High-Entropy Alloys*, Springer International Publishing, Cham, 2016, pp. 1–19, https://doi.org/10.1007/978-3-319-27013-5_1.
- [11] Z. Li, K.G. Pradeep, Y. Deng, D. Raabe, C.C. Tasan, Metastable high-entropy dual-phase alloys overcome the strength–ductility trade-off, *Nature* 534 (2016) 227–230, <https://doi.org/10.1038/nature17981>.
- [12] Z. Zhang, M.M. Mao, J. Wang, B. Gludovatz, Z. Zhang, S.X. Mao, E.P. George, Q. Yu, R.O. Ritchie, Nanoscale origins of the damage tolerance of the high-entropy alloy CrMnFeCoNi, *Nat. Commun.* 6 (2015) 10143, <https://doi.org/10.1038/ncomms10143>.
- [13] M. Chuang, M. Tsai, W. Wang, S. Lin, J. Yeh, Microstructure and wear behavior of AlxCu1.5CrFeNi1.5Ti high-entropy alloys, *Acta Mater.* 59 (2011) 6308–6317, <https://doi.org/10.1016/j.actamat.2011.06.041>.
- [14] Y. Shi, L. Collins, R. Feng, C. Zhang, N. Balke, P.K. Liaw, B. Yang, Homogenization of Al CoCrFeNi high-entropy alloys with improved corrosion resistance, *Corros. Sci.* 133 (2018) 120–131, <https://doi.org/10.1016/j.corsci.2018.01.030>.
- [15] Y.Y. Chen, U.T. Hong, H.C. Shih, J.W. Yeh, T. Duval, Electrochemical kinetics of the high entropy alloys in aqueous environments—a comparison with type 304 stainless steel, *Corros. Sci.* 47 (2005) 2679–2699, <https://doi.org/10.1016/j.corsci.2004.09.026>.
- [16] O.N. Senkov, C.F. Woodward, Microstructure and properties of a refractory NbCrMo0.5Ta0.5TiZr alloy, *Mater. Sci. Eng.: A* 529 (2011) 311–320, <https://doi.org/10.1016/j.msea.2011.09.033>.
- [17] Y. Zhang, High-Entropy Materials: Advances and Applications, 1st ed., CRC Press, Boca Raton, 2023 <https://doi.org/10.1201/9781003319986>.
- [18] C.M. Hansson, The impact of corrosion on society, *Met. Mater. Trans. A* 42 (2011) 2952–2962, <https://doi.org/10.1007/s11661-011-0703-2>.
- [19] O.N. Senkov, S.V. Senkova, C. Woodward, Effect of aluminum on the microstructure and properties of two refractory high-entropy alloys, *Acta Mater.* 68 (2014) 214–228, <https://doi.org/10.1016/j.actamat.2014.01.029>.
- [20] W. Wu, Z. Liu, Q. Wang, X. Li, Improving the resistance of high-strength steel to SCC in a SO₂-polluted marine atmosphere through Nb and Sb microalloying, *Corros. Sci.* 170 (2020) 108693, <https://doi.org/10.1016/j.corsci.2020.108693>.
- [21] Y. Hsu, W. Chiang, J. Wu, Corrosion behavior of FeCoNiCrCu_x high-entropy alloys in 3.5% sodium chloride solution, *Mater. Chem. Phys.* 92 (2005) 112–117, <https://doi.org/10.1016/j.matchemphys.2005.01.001>.
- [22] M. Wang, Z. Wen, J. Liu, J. Wang, Z. Wu, J. Qin, Y. Zhao, Synergistic effect of Zr and Hf alloying on cross fluvial microstructure of CoCrFeNi eutectic high-entropy alloys, *Mater. Lett.* 345 (2023) 134416, <https://doi.org/10.1016/j.matlet.2023.134416>.
- [23] P. Lyu, Y. Chen, Z. Liu, J. Cai, C. Zhang, Y. Jin, Q. Guan, N. Zhao, Surface modification of CrFeCoNiMo high entropy alloy induced by high-current pulsed electron beam, *Appl. Surf. Sci.* 504 (2020) 144453, <https://doi.org/10.1016/j.apsusc.2019.144453>.
- [24] A. Tanji, R. Feng, Z. Lyu, R. Sakidja, P.K. Liaw, H. Hermawan, Passivity of AlCrFeNiTi and AlCrFeCoNi high-entropy alloys in Hanks' solution, *Corros. Sci.* 210 (2023) 110828, <https://doi.org/10.1016/j.corsci.2022.110828>.
- [25] Y. Shi, B. Yang, X. Jie, T. Brecht, K.A. Dahmen, P.K. Liaw, Corrosion of Al CoCrFeNi high-entropy alloys: Al-content and potential scan-rate dependent pitting behavior, *Corros. Sci.* 119 (2017) 33–45, <https://doi.org/10.1016/j.corsci.2017.02.019>.
- [26] Q. Zhao, Z. Pan, X. Wang, H. Luo, Y. Liu, X. Li, Corrosion and passive behavior of AlxCrFeNi_{3-x} (x = 0.6, 0.8, 1.0) eutectic high entropy alloys in chloride environment, *Corros. Sci.* 208 (2022) 110666, <https://doi.org/10.1016/j.corsci.2022.110666>.
- [27] J. Wang, H. Jiang, X. Chang, L. Zhang, H. Wang, L. Zhu, S. Qin, Effect of Cu content on the microstructure and corrosion resistance of AlCrFeNi3Cu_x high entropy alloys, *Corros. Sci.* 221 (2023) 111313, <https://doi.org/10.1016/j.corsci.2023.111313>.
- [28] C. Liu, Y. Gao, K. Chong, F. Guo, D. Wu, Y. Zou, Effect of Nb content on the microstructure and corrosion resistance of FeCoCrNiNb_x high-entropy alloys in chloride ion environment, *J. Alloy. Compd.* 935 (2023) 168013, <https://doi.org/10.1016/j.jallcom.2022.168013>.
- [29] L.B. Chen, R. Wei, K. Tang, J. Zhang, F. Jiang, L. He, J. Sun, Heavy carbon alloyed FCC-structured high entropy alloy with excellent combination of strength and ductility, *Mater. Sci. Eng. A* 716 (2018) 150–156, <https://doi.org/10.1016/j.msea.2018.01.045>.
- [30] S. Wu, D. Qiao, H. Zhang, J. Miao, H. Zhao, J. Wang, Y. Lu, T. Wang, T. Li, Microstructure and mechanical properties of CxHf0.25NbTaW0.5 refractory high-entropy alloys at room and high temperatures, *J. Mater. Sci. Technol.* 97 (2022) 229–238, <https://doi.org/10.1016/j.jmst.2021.05.015>.
- [31] T. Barrès, B. Tribollet, O. Stephan, H. Montigaud, M. Boinet, Y. Cohin, Characterization of the porosity of silicon nitride thin layers by Electrochemical Impedance Spectroscopy, *Electrochim. Acta* 227 (2017) 1–6, <https://doi.org/10.1016/j.electacta.2017.01.008>.
- [32] M. Traversier, P. Mestre-Rinn, N. Peillon, E. Rigal, X. Boulnat, F. Tancret, J. Dhers, A. Fraczkiewicz, Nitrogen-induced hardening in an austenitic CrFeMnNi high-entropy alloy (HEA), *Mater. Sci. Eng. A* 804 (2021) 140725, <https://doi.org/10.1016/j.msea.2020.140725>.
- [33] Y. Chen, Y. Li, X. Cheng, Z. Xu, C. Wu, B. Cheng, M. Wang, Interstitial strengthening of refractory ZrTiHfNb0.5Ta0.5O_x (x = 0.05, 0.1, 0.2) high-entropy alloys, *Mater. Lett.* 228 (2018) 145–147, <https://doi.org/10.1016/j.matlet.2018.05.123>.
- [34] Z. Lei, X. Liu, Y. Wu, H. Wang, S. Jiang, S. Wang, X. Hui, Y. Wu, B. Gault, P. Kontis, D. Raabe, L. Gu, Q. Zhang, H. Chen, H. Wang, J. Liu, K. An, Q. Zeng, T.-G. Nieh, Z. Lu, Enhanced strength and ductility in a high-entropy alloy via ordered oxygen complexes, *Nature* 563 (2018) 546–550, <https://doi.org/10.1038/s41586-018-0685-y>.
- [35] Y. Xie, H. Cheng, Q. Tang, W. Chen, W. Chen, P. Dai, Effects of N addition on microstructure and mechanical properties of CoCrFeNiMn high entropy alloy produced by mechanical alloying and vacuum hot pressing sintering, *Intermetallics* 93 (2018) 228–234, <https://doi.org/10.1016/j.intermet.2017.09.013>.
- [36] L.J. Zhang, P.F. Yu, J.T. Fan, M.D. Zhang, C.Z. Zhang, H.Z. Cui, G. Li, Investigating the micro and nanomechanical properties of CoCrFeNi-C high-entropy alloys containing eutectic carbides, *Mater. Sci. Eng.: A* 796 (2020) 140065, <https://doi.org/10.1016/j.msea.2020.140065>.
- [37] S.D. Carpenter, D. Carpenter, X-ray diffraction study of M7C3 carbide within a high chromium white iron, *Mater. Lett.* 57 (2003) 4456–4459, [https://doi.org/10.1016/S0167-577X\(03\)00342-2](https://doi.org/10.1016/S0167-577X(03)00342-2).
- [38] L.J. Zhang, Z.K. Jiang, M.D. Zhang, J.T. Fan, D.J. Liu, P.F. Yu, G. Li, R.P. Liu, Effect of solid carburization on the surface microstructure and mechanical properties of the equiatomic CoCrFeNi high-entropy alloy, *J. Alloy. Compd.* 769 (2018) 27–36, <https://doi.org/10.1016/j.jallcom.2018.07.329>.
- [39] Y.L. Chou, Y.C. Wang, J.W. Yeh, H.C. Shih, Pitting corrosion of the high-entropy alloy Co1.5CrFeNi1.5Ti0.5Mo0.1 in chloride-containing sulphate solutions, *Corros. Sci.* 52 (2010) 3481–3491, <https://doi.org/10.1016/j.corsci.2010.06.025>.
- [40] S. Jiang, Z. Lin, H. Xu, Y. Sun, Studies on the microstructure and properties of AlxCrCoFeNiTi1-x high entropy alloys, *J. Alloy. Compd.* 741 (2018) 826–833, <https://doi.org/10.1016/j.jallcom.2018.01.247>.
- [41] X.-Z. Wang, H. Luo, J.-L. Luo, Effects of hydrogen and stress on the electrochemical and passivation behaviour of 304 stainless steel in simulated PEMFC environment, *Electrochim. Acta* 293 (2019) 60–77, <https://doi.org/10.1016/j.electacta.2018.10.028>.
- [42] D. Wallinder, J. Pan, C. Leygraf, A. Delblanc-Bauer, Eis and XPS study of surface modification of 316LVM stainless steel after passivation, *Corros. Sci.* 41 (1998) 275–289, [https://doi.org/10.1016/S0010-938X\(98\)00122-X](https://doi.org/10.1016/S0010-938X(98)00122-X).
- [43] K. Feng, Y. Zhang, Z. Li, C. Yao, L. Yao, C. Fan, Corrosion properties of laser cladded CrCoNi medium entropy alloy coating, *Surf. Coat. Technol.* 397 (2020) 126004, <https://doi.org/10.1016/j.surcoat.2020.126004>.
- [44] L. Chen, W. Liu, B. Dong, Y. Zhao, T. Zhang, Y. Fan, W. Yang, Insight into electrochemical passivation behavior and surface chemistry of 2205 duplex stainless steel: effect of tensile elastic stress, *Corros. Sci.* 193 (2021) 109903, <https://doi.org/10.1016/j.corsci.2021.109903>.
- [45] G. Song, A.L. Bowles, D.H. StJohn, Corrosion resistance of aged die cast magnesium alloy AZ91D, *Mater. Sci. Eng.: A* 366 (2004) 74–86, <https://doi.org/10.1016/j.msea.2003.08.060>.
- [46] L. Jinlong, L. Hongyun, Effect of surface burnishing on texture and corrosion behavior of 2024 aluminum alloy, *Surf. Coat. Technol.* 235 (2013) 513–520, <https://doi.org/10.1016/j.surcoat.2013.07.071>.
- [47] F. Bentiss, C. Jama, B. Mernari, H.E. Attari, L.E. Kadi, M. Lebrini, M. Traisnel, M. Lagrenée, Corrosion control of mild steel using 3,5-bis(4-methoxyphenyl)-4-amino-1,2,4-triazole in normal hydrochloric acid medium, *Corros. Sci.* 51 (2009) 1628–1635, <https://doi.org/10.1016/j.corsci.2009.04.009>.
- [48] H. Luo, S. Zou, Y.-H. Chen, Z. Li, C. Du, X. Li, Influence of carbon on the corrosion behaviour of interstitial equiatomic CoCrFeMnNi high-entropy alloys in a chlorinated concrete solution, *Corros. Sci.* 163 (2020) 108287, <https://doi.org/10.1016/j.corsci.2019.108287>.
- [49] B. Lynch, S. Neupane, F. Wiame, A. Seyeux, V. Maurice, P. Marcus, An XPS and ToF-SIMS study of the passive film formed on a model FeCrNiMo stainless steel surface in aqueous media after thermal pre-oxidation at ultra-low oxygen pressure, *Appl. Surf. Sci.* 554 (2021) 149435, <https://doi.org/10.1016/j.apsusc.2021.149435>.
- [50] L.-Y. Chen, H.-Y. Zhang, C. Zheng, H.-Y. Yang, P. Qin, C. Zhao, S. Lu, S.-X. Liang, L. Chai, L.-C. Zhang, Corrosion behavior and characteristics of passive films of laser powder bed fusion produced Ti-6Al-4V in dynamic Hank's solution, *Mater. Des.* 208 (2021) 109907, <https://doi.org/10.1016/j.matdes.2021.109907>.
- [51] P. Yi, D. Chen, M. Li, Z. Yang, Z. Fang, J. Mo, K. Xiao, C. Dong, Effect of Nd addition on the corrosion behavior of SAC305 solder alloy, *Corros. Sci.* 220 (2023) 111264, <https://doi.org/10.1016/j.corsci.2023.111264>.
- [52] M. Gaberšček, S. Pejovnik, Impedance spectroscopy as a technique for studying the spontaneous passivation of metals in electrolytes, *Electrochim. Acta* 41 (1996) 1137–1142, [https://doi.org/10.1016/0013-4686\(95\)00464-5](https://doi.org/10.1016/0013-4686(95)00464-5).
- [53] Q. Liu, H. Liu, J. Xie, W. Zhang, Y. Zhang, C. Feng, G. Li, Y. Yu, S. Song, C. Yin, Influence of Ru on structure and corrosion behavior of passive film on Ti-6Al-4V alloy in oil and gas exploration conditions, *Sci. Rep.* 12 (2022) 16586, <https://doi.org/10.1038/s41598-022-21047-0>.

- [54] J. Wang, D. Li, T. Shao, Diffusivity of point defects in the passive film on a Ni16Cr13Co4Mo alloy in molten NaCl-Na2SO4, *Corros. Sci.* 223 (2023) 111456, <https://doi.org/10.1016/j.corsci.2023.111456>.
- [55] H. Liu, H. Liu, S. Zhang, H. Wang, X. Wei, L. Ren, K. Yang, Metastable pitting corrosion behavior of laser powder bed fusion produced Ti6Al4V-Cu in 3.5% NaCl solution, *Corros. Sci.* 223 (2023) 111452, <https://doi.org/10.1016/j.corsci.2023.111452>.
- [56] P. Qin, H. Ma, Y. Cui, R. Liu, P. Ju, F. Wang, L. Liu, The corrosion behavior of 316 stainless steel under the cooperative effect of plastic stress and UV illumination in 3.5 wt% NaCl solution, *Corros. Sci.* 223 (2023) 111466, <https://doi.org/10.1016/j.corsci.2023.111466>.
- [57] B. Hirschorn, M.E. Orazem, B. Tribollet, V. Vivier, I. Frateur, M. Musiani, Determination of effective capacitance and film thickness from constant-phase-element parameters, *Electrochim. Acta* 55 (2010) 6218–6227, <https://doi.org/10.1016/j.electacta.2009.10.065>.
- [58] M.E. Orazem, I. Frateur, B. Tribollet, V. Vivier, S. Marcellin, N. Pébere, A.L. Bunge, E.A. White, D.P. Riemer, M. Musiani, Dielectric properties of materials showing constant-phase-element (CPE) impedance response, *J. Electrochem. Soc.* 160 (2013) C215–C225, <https://doi.org/10.1149/2.03330ejes>.
- [59] G.J. Brug, A.L.G. van den Eeden, M. Sluyters-Rehbach, J.H. Sluyters, The analysis of electrode impedances complicated by the presence of a constant phase element, *J. Electroanal. Chem. Interfacial Electrochem.* 176 (1984) 275–295, [https://doi.org/10.1016/S0022-0728\(84\)80324-1](https://doi.org/10.1016/S0022-0728(84)80324-1).
- [60] Z. Cui, S. Chen, Y. Dou, S. Han, L. Wang, C. Man, X. Wang, S. Chen, Y.F. Cheng, X. Li, Passivation behavior and surface chemistry of 2507 super duplex stainless steel in artificial seawater: Influence of dissolved oxygen and pH, *Corros. Sci.* 150 (2019) 218–234, <https://doi.org/10.1016/j.corsci.2019.02.002>.
- [61] E. Gileadi, Anomalous temperature dependence of the tafel slope, *J. Electrochem. Soc.* 134 (1987) 117, <https://doi.org/10.1149/1.2100386>.
- [62] B. Hirschorn, M.E. Orazem, B. Tribollet, V. Vivier, I. Frateur, M. Musiani, Constant-phase-element behavior caused by resistivity distributions in films, *J. Electrochem. Soc.* 28 (2010) 77, <https://doi.org/10.1149/1.3496423>.
- [63] Z. Cui, L. Wang, H. Ni, W. Hao, C. Man, S. Chen, X. Wang, Z. Liu, X. Li, Influence of temperature on the electrochemical and passivation behavior of 2507 super duplex stainless steel in simulated desulfurized flue gas condensates, *Corros. Sci.* 118 (2017) 31–48, <https://doi.org/10.1016/j.corsci.2017.01.016>.
- [64] X. Wan, A. Lan, M. Zhang, X. Jin, H. Yang, J. Qiao, Corrosion and passive behavior of Al0.8CrFeNi2.2 eutectic high entropy alloy in different media, *J. Alloy. Compd.* 944 (2023) 169217, <https://doi.org/10.1016/j.jallcom.2023.169217>.
- [65] R.M. Fernández-Domene, E. Blasco-Tamarit, D.M. García-García, J. García-Antón, Passive and transpassive behaviour of Alloy 31 in a heavy brine LiBr solution, *Electrochim. Acta* 95 (2013) 1–11, <https://doi.org/10.1016/j.electacta.2013.02.024>.
- [66] A. Fattah-alhosseini, M.A. Golozar, A. Saatchi, K. Raeissi, Effect of solution concentration on semiconducting properties of passive films formed on austenitic stainless steels, *Corros. Sci.* 52 (2010) 205–209, <https://doi.org/10.1016/j.corsci.2009.09.003>.
- [67] J. Yao, D.D. Macdonald, C. Dong, Passive film on 2205 duplex stainless steel studied by photo-electrochemistry and ARXPS methods, *Corros. Sci.* 146 (2019) 221–232, <https://doi.org/10.1016/j.corsci.2018.10.020>.
- [68] A. Hankin, F.E. Bedoya-Lora, J.C. Alexander, A. Regoutz, G.H. Kelsall, Flat band potential determination: avoiding the pitfalls, *J. Mater. Chem. A* 7 (2019) 26162–26176, <https://doi.org/10.1039/C9TA09569A>.
- [69] Y. Zhang, M. Urquidi-Macdonald, G.R. Engelhardt, D.D. Macdonald, Development of localized corrosion damage on low pressure turbine disks and blades: I. Passivity, *Electrochim. Acta* 69 (2012) 1–11, <https://doi.org/10.1016/j.electacta.2012.01.022>.
- [70] E. Sikora, J. Sikora, D.D. Macdonald, A new method for estimating the diffusivities of vacancies in passive films, *Electrochim. Acta* 41 (1996) 783–789, [https://doi.org/10.1016/0013-4686\(95\)00312-6](https://doi.org/10.1016/0013-4686(95)00312-6).
- [71] B. Munirathinam, R. Narayanan, L. Neelakantan, Electrochemical and semiconducting properties of thin passive film formed on titanium in chloride medium at various pH conditions, *Thin Solid Films* 598 (2016) 260–270, <https://doi.org/10.1016/j.tsf.2015.12.025>.
- [72] Y.F. Cheng, C. Yang, J.L. Luo, Determination of the diffusivity of point defects in passive films on carbon steel, *Thin Solid Films* 416 (2002) 169–173, [https://doi.org/10.1016/S0040-6090\(02\)00617-X](https://doi.org/10.1016/S0040-6090(02)00617-X).
- [73] K.-M. Hsu, S.-H. Chen, C.-S. Lin, Microstructure and corrosion behavior of FeCrNiCoMnx ($x = 1.0, 0.6, 0.3, 0$) high entropy alloys in 0.5 M H₂SO₄, *Corros. Sci.* 190 (2021) 109694, <https://doi.org/10.1016/j.corsci.2021.109694>.
- [74] C.-O.A. Olson, D. Landolt, Passive films on stainless steels—chemistry, structure and growth, *Electrochim. Acta* 48 (2003) 1093–1104, [https://doi.org/10.1016/S0013-4686\(02\)00841-1](https://doi.org/10.1016/S0013-4686(02)00841-1).
- [75] Y. Shi, L. Collins, N. Balke, P.K. Liaw, B. Yang, In-situ electrochemical-AFM study of localized corrosion of AlxCoCrFeNi high-entropy alloys in chloride solution, *Appl. Surf. Sci.* 439 (2018) 533–544, <https://doi.org/10.1016/j.apsusc.2018.01.047>.
- [76] H. Luo, H. Su, C. Dong, X. Li, Passivation and electrochemical behavior of 316L stainless steel in chlorinated simulated concrete pore solution, *Appl. Surf. Sci.* 400 (2017) 38–48, <https://doi.org/10.1016/j.apsusc.2016.12.180>.
- [77] Y. Wang, S.L. Jiang, Y.G. Zheng, W. Ke, W.H. Sun, J.Q. Wang, Effect of porosity sealing treatments on the corrosion resistance of high-velocity oxy-fuel (HVOF)-sprayed Fe-based amorphous metallic coatings, *Surf. Coat. Technol.* 206 (2011) 1307–1318, <https://doi.org/10.1016/j.surfcoat.2011.08.045>.
- [78] B. Zhang, J. Wang, B. Wu, X.W. Guo, Y.J. Wang, D. Chen, Y.C. Zhang, K. Du, E. E. Oguzie, X.L. Ma, Unmasking chloride attack on the passive film of metals, *Nat. Commun.* 9 (2018) 2559, <https://doi.org/10.1038/s41467-018-04942-x>.
- [79] J. Ma, B. Zhang, Y. Fu, X. Hu, X. Cao, Z. Pan, Y. Wei, H. Luo, X. Li, Effect of cold deformation on corrosion behavior of selective laser melted 316L stainless steel bipolar plates in a simulated environment for proton exchange membrane fuel cells, *Corros. Sci.* 201 (2022) 110257, <https://doi.org/10.1016/j.corsci.2022.110257>.
- [80] Z.B. Zheng, Y.G. Zheng, Effects of surface treatments on the corrosion and erosion-corrosion of 304 stainless steel in 3.5% NaCl solution, *Corros. Sci.* 112 (2016) 657–668, <https://doi.org/10.1016/j.corsci.2016.09.005>.
- [81] C. Dai, T. Zhao, C. Du, Z. Liu, D. Zhang, Effect of molybdenum content on the microstructure and corrosion behavior of FeCoCrNiMox high-entropy alloys, *J. Mater. Sci. Technol.* 46 (2020) 64–73, <https://doi.org/10.1016/j.jmst.2019.10.020>.
- [82] G.T. Burstein, P.C. Pistorius, S.P. Mattin, The nucleation and growth of corrosion pits on stainless steel, *Corros. Sci.* 35 (1993) 57–62, [https://doi.org/10.1016/0010-938X\(93\)90133-2](https://doi.org/10.1016/0010-938X(93)90133-2).